CHALMERS

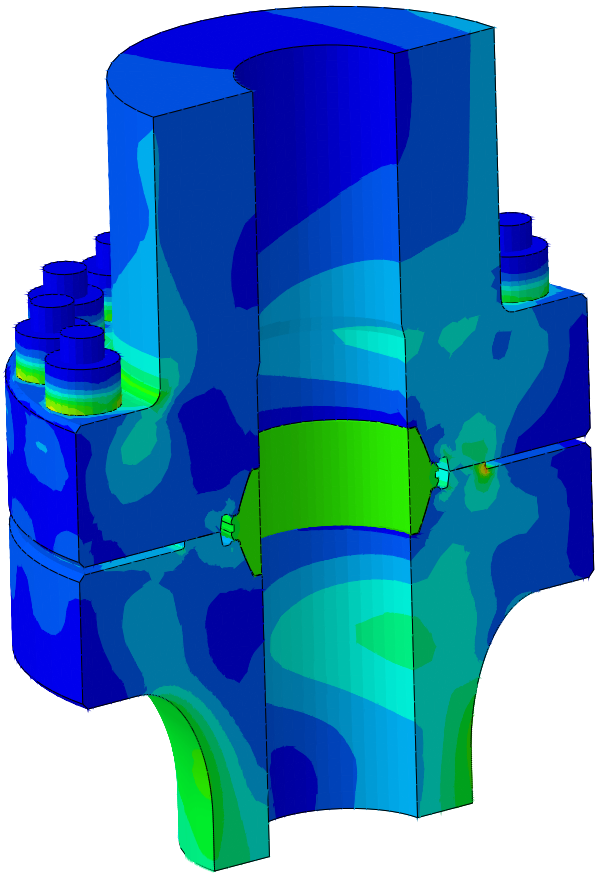

Structural and functional capacity evaluation of a flange with/without a raised face

Master's thesis in Applied Mechanics

MOHSEN SAFDARY
SAMI MASOUMZADEH

Department of Applied Mechanics
CHALMERS UNIVERSITY OF TECHNOLOGY
Göteborg, Sweden 2015

MASTER'S THESIS IN APPLIED MECHANICS

Structural and functional capacity evaluation of a flange with/without a raised face

MOHSEN SAFDARY
SAMI MASOUMZADEH

Department of Applied Mechanics
Division of Material and Computational Mechanics
CHALMERS UNIVERSITY OF TECHNOLOGY

Göteborg, Sweden 2015

Structural and functional capacity evaluation of a flange with/without a raised face
MOHSEN SAFDARY
SAMI MASOUMZADEH

Master's thesis 2015:28
ISSN 1652-8557
Department of Applied Mechanics
Division of Material and Computational Mechanics
Chalmers University of Technology
SE-412 96 Göteborg
Sweden
Telephone: +46 (0)31-772 1000

Cover:
The von Mises stress field for the raised face flange when subjected to a bending moment.

Chalmers Reproservice
Göteborg, Sweden 2015

Structural and functional capacity evaluation of a flange with/without a raised face
Master's thesis in Applied Mechanics
MOHSEN SAFDARY
SAMI MASOUMZADEH
Department of Applied Mechanics
Division of Material and Computational Mechanics
Chalmers University of Technology

Abstract

The offshore equipment for the oil and gas industry provided by Aker Solutions is subjected to both environmental as well as functional loads. It is of crucial importance that the components can withstand these loads without any risk of failure or leakage.

Two geometrically different bolted flanges; one with and the other without a raised hub face, denoted flat face were provided by Aker Solutions. These two flanges were analysed using the finite element software Abaqus. The aim was to compare the performances of the two flanges in order to identify major differences in capacities. The flanges were subjected to separate loads in tension, bending and internal pressure. Capacities based on structural and functional criteria as well as a fatigue assessment according to industrial standards were evaluated and the results for the two flanges were compared with each other.

No major differences could be seen between the flanges when evaluating the structural capacities in tension and in internal pressure. However, when subjected to bending, the flat face flange could withstand a higher bending moment compared to the raised face flange. The same behaviour could be seen for the functional capacities; when loaded in tension or internal pressure the flanges performed equal, but when loaded in bending the flat face flange performed significantly better. When subjected to a cyclic fatigue load in bending, the flanges exhibited similar results.

The conclusion drawn from the results is that the capacity of the flat face flange are superior to that of the raised face flange when evaluated according to the present criteria and methods.

Keywords: Bolted flange joints, Raised face, Abaqus, Bolts, Submodel, Offshore.

Preface

This masters thesis project was done under the time period of spring 2015 as a final course in the Applied Mechanics master program at Chalmers University of Technology. The project was carried out at the analytics division of the consultant company Alten in Gothenburg for Aker Solutions in Oslo.

Acknowledgements

We would like to thank Prof. Lennart Josefson at Chalmers University of Technology for being our academic supervisor and examiner and setting up our access to the Chalmers cluster. Thanks to PhD. student Senad Razanica for his quick tutorial on the Chalmers cluster. Additional gratitude to our supervisor Mikael Almquist and the people at Alten for supporting us and providing a pleasant working environment. Last but not least thanks to Tobias Tivert and his colleges at Aker Solutions for giving us an interesting master thesis and answering our many questions. Thanks also to co-students Christian, Maham, Simon and Robin for keeping up the spirit during the masters thesis project time.

This assignment has been a great opportunity for us to apply the knowledge we earned during our study years as well as a suitable transition from the academic student life to the industrial work life.

Göteborg, June 2015

Mohsen Safdary

Sami Masoumzadeh

Contents

1 Introduction

1.1 Background

Bolted flange connections are a widely used mechanical component in areas such as the nuclear, chemical and in this present case, the oil and gas industry. Bolted flange joints are commonly used in hydraulic systems when joining individual elements such as pipes and pipelines. In the offshore industry, the flange connections are used to connect the vertical pipelines, denoted risers, to the well heads on the seabed as well as connecting the risers to the surface flow trees. Due to the common use of the flange joints, existing work, both analytical [1] as well as numerical [1][2][3][4][5][6] and experimental [1][3][4], for similar applications, mainly the pressure distribution in the gasket and sealing performance exists. The gasket types in these cases have consisted of regular flat gaskets.

The equipment and components used in the offshore industry are subjected to high loads and a tough environment. It is of importance that the components can stand the impact while simultaneously assuring functionality without risk of failure or leakage, even under the most extreme circumstances. Due to the high operational costs, it is also of importance to keep downtime and costs to a minimum. To govern the methods used when designing the components, several best practice reports and industrial standards such as ISO 13628 [7], Statoil's TR 3541 [8] and DNV RP-C203 [9] exist. ISO 13628 gives guidance, general requirements and recommendations for development of subsea production systems, part 7 of this report covers completion/workover riser systems. TR 3541 is Statoil's specification requirements on subsea Xmas trees and completion/workover systems. DNV RP-C230 provides recommendations on fatigue design analysis based on fatigue tests. In addition, several internal company interpretations that serve as guidance exists.

Aker Solutions is a globally supplying company for equipment and services used in the oil and gas industry. The products are governed by strict regulations to ensure the intended functionality. One of Aker Solutions various products consists of flange connections. Environmental influences such as waves, currents and winds as well as operational loads consisting of internal overpressure, bending and pulling will result in locally high stresses. The various loads will also affect the contact pressure between the flange hub faces, as presented in [4]. It is crucial that the flanges can withstand these loads without any risk of leakage or failure. High loads resulting in both material and geometrical nonlinearity as well as complex geometries and numerous components demand the use of numerical methods, e.g. finite element method (FEM).

One of the weak points of the flange connection is the assembly bolts [10]. In order to create and maintain the contact pressure the bolts are pretensioned, resulting in initial bolt stresses before any external load is applied. Additionally external loads as well as flange rotation due to flexural flexibility results in tension and bending of the bolts. Due to the high loads, the bolts are often made of high strength steel. It is known that high strength materials are more sensitive to fatigue [11][12]. This, in addition to the stress concentrations in the thread roots, motivates a fatigue assessment for the bolts and flange, as recommended in ISO 13628-7 [7]; "Fatigue-sensitive points shall be identified and a fatigue analysis shall be performed for each point. Emphasis should be on bolts, welds and details with stress concentrations, in addition to locations with high surface roughness and surface marks.".

Bolted flanges are a complex area where a lot of parameters need to be considered. Different kinds of bolted flanges are used in the subsea industry, one widely used is the standard American Petroleum Institute (API) flange. The most commonly used is flange with a raised hub face and a complementary spherical titanium TX seal. Earlier versions of the flange used a smaller ring shaped BX seal. The small BX seal demanded a raised hub face flange in order to obtain a proper pressure on the seal. When the BX seal was replaced with the TX seal the assumption of the need of a raised face on the flange remained. An alternative to the raised face flange is a flange with a completely flat hub face, denoted flat face flange. Questions that arise: Are there any disadvantages with the raised face as compared with a completely flat hub face? How does the performance differ between the flanges?

1.2 Purpose

The purpose of this project is to investigate the difference in structural and functional capacities as well as fatigue properties between a raised hub face flange and a flat hub face flange using finite element analysis (FEA). The analyses will be evaluated according to industrial and Aker Solutions internal criteria. The results will contribute to a better understanding of the parameters that are important when designing flanges.

1.3 Objectives

More specifically the objective of the project has been to first establish criteria based on industrial standards that can be used for evaluating the capacities. In addition to this, the objective has been to implement the geometry in the FEA software Abaqus with proper modelling assumptions. Lastly, the objective has been to interpret the results in order to evaluate the capacities.

1.4 Limitations

The limitations of the project have been determined by examination of the project description, previous work done by Aker Solutions, and in discussion with the supervisors. Since the purpose of the project is to compare the performance of the flanges, no variation of temperature, friction or bolt preload will be studied. Only pure cases of the structural capacities will be evaluated, meaning that when analysing the capacity in tension, no bending or pressure will be applied. The fatigue analysis will only consider the case of pure bending.

Due to computational cost, the threads of the bolts will not be modelled separately. Instead different contact interactions and couplings will be used. This is a non-conservative approach since the roots of the threads act as stress raisers and cracks initiate at the thread roots [7][13]. When analysing the loss of pretension, only one load cycle will be evaluated for each step. Meaning that the flange is restored to its initial material state after each load. No temperature variation will be applied and all material properties will be used for the steady temperature of 121 °C, a maximum temperature commonly used in subsea applications. No consideration will be done for galling or adhesive wear between parts during cyclic loads. Environmental effects such as corrosion, hydrogen induced cracking or sour service will not be taking into account.

1.5 Thesis outline

This master thesis report is divided into 5 chapters. The first chapter, this present one, presents the project definition and a brief associated background. The second chapter presents the underlying theory used in the computational software. It includes the finite element formulation, nonlinear equation solving using Newton's method, material modelling, contact theory and a short explanation of how fatigue is analysed. Chapter 3 describes the methodology for the analysis. It contains the necessary steps done to implement the model in the software. The criteria used to evaluate the capacities are also defined in this chapter. Chapter 4 presents the results from the analysis together with a discussion of the results. The final chapter is a conclusion of the results. It summarizes the project and its results and gives recommendations for future work.

2 Theory

In this chapter, the basic steps of the finite element method are presented in more general, for a more detailed explanation, examine a introductory textbook such as Ottoson & Peterssons "Introduction to the Finite Element Method" [14]. Additionally, the behaviour of the material when yielding is also described. The two most commonly used methods for solving contact problems are also explained. Further, different methods for fatigue life assessment are presented.

2.1 Finite Element method

The finite element method, (FEM), is a numerical method for solving problems of engineering and mathematical physics. The method has been applied to a number of physical problems where the governing differential equations are available. The method essentially consists of discretization of the problem assuming a piecewise continuous function for the solution and obtaining the parameters of the functions in a manner that reduces the error in the solution. The method is very useful for problems with complicated geometries, loadings, and material properties where analytical solutions can not be obtained. Figure 2.1 summarises all the steps used in the FEM.

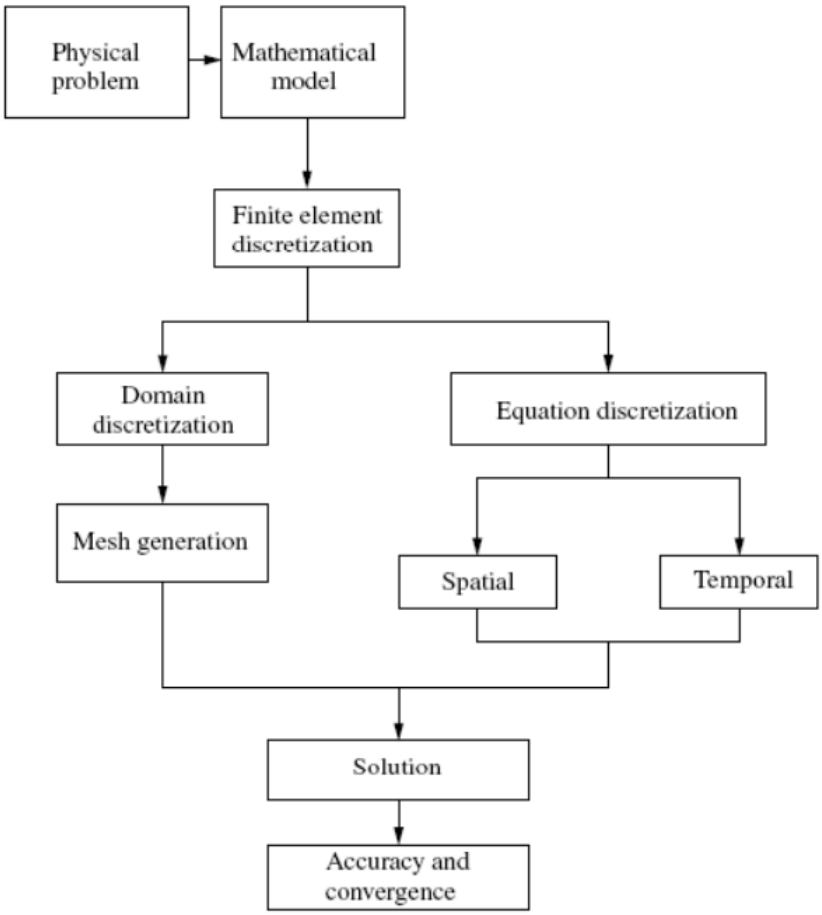

Figure 2.1: *FEM steps.*

2.1.1 Governing equations

Consider a body with domain Ω, fig. 2.2. The domain is bounded by the boundary Γ. The boundary can be divided into four sets; Γ_1, Γ_2, Γ_u where the displacement $\boldsymbol{u}$ is prescribed and Γ_σ where a traction force $\boldsymbol{t}$ is applied.

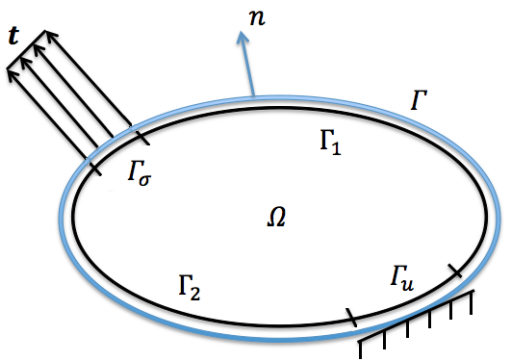

Figure 2.2: *Body with domain* Ω *and boundary* Γ.

The equilibrium equation and boundary conditions are:

$$-\tilde{\boldsymbol{\nabla}}^{\boldsymbol{T}}\,\boldsymbol{\sigma} = \boldsymbol{b} \tag{2.1}$$

$$\boldsymbol{\sigma} = \boldsymbol{\sigma}(\boldsymbol{\epsilon}[\boldsymbol{u}]) \tag{2.2}$$

$$\boldsymbol{\sigma}\,\boldsymbol{n} = \boldsymbol{t} \qquad on\ \Gamma_\sigma \tag{2.3}$$

$$\boldsymbol{u} = \boldsymbol{u}_{\boldsymbol{prescribed}} \qquad on\ \Gamma_u \tag{2.4}$$

where $\boldsymbol{n}$ is the normal vector of the boundary. By multiplying the equilibrium equation by an arbitrary test function, $\delta\boldsymbol{v}$, integrating over the domain Ω and using the boundary conditions, the corresponding Voigt format of the weak form is obtained as

$$\int_\Omega (\tilde{\boldsymbol{\nabla}}\delta\boldsymbol{v})^T\boldsymbol{\sigma} = \int_{\Gamma_\sigma} (\delta\boldsymbol{v})^T\ \boldsymbol{t}\ d\Gamma + \int_\Omega (\delta\boldsymbol{v})^T\ \boldsymbol{b}\ d\Omega \tag{2.5}$$

2.1.2 FE-approximation

The weak format of equilibrium, eq. (2.5), is used to formulate the finite element approximation. The displacement function $\boldsymbol{u}$ can be approximated as:

$$\boldsymbol{u}(x,y,z) \approx \boldsymbol{u_h}(x,y,z) = \sum_{i=1}^{N_{DOF}} N_i(x,y,z)u_i = \boldsymbol{N}(x,y,z)\ \boldsymbol{a} \tag{2.6}$$

where $\boldsymbol{N}$ is the shape functions

$$\boldsymbol{N} = \begin{bmatrix} N_1 & 0 & 0 & \cdots & N_{ndof} & 0 & 0 \\ 0 & N_1 & 0 & \cdots & 0 & N_{ndof} & 0 \\ 0 & 0 & N_1 & \cdots & 0 & 0 & N_{ndof} \end{bmatrix}$$

and $\boldsymbol{a}$ is the nodal displacement vector

$$\boldsymbol{a} = \begin{bmatrix} u_{x,1} & u_{y,1} & u_{z,1} & \cdots & u_{x,ndof} & u_{y,ndof} & u_{z,ndof} \end{bmatrix}^T$$

Including the constitutive relation and using eq. (2.6) the strain $\boldsymbol{\epsilon}$ can be evaluated as

$$\boldsymbol{\epsilon}(x,y,z) = \tilde{\boldsymbol{\nabla}}\boldsymbol{u}(x,y,z) = \tilde{\boldsymbol{\nabla}}\boldsymbol{N}(x,y,z)a = \boldsymbol{B}(x,y,z)\boldsymbol{a} \tag{2.7}$$

This gives that $\boldsymbol{\sigma}(\boldsymbol{\epsilon}) = \boldsymbol{DBa}$, where $\boldsymbol{D}$ is the constitutive matrix. According to the Galerkin method [15], the test function $\delta\boldsymbol{v} = \boldsymbol{Nc}$, where the matrix $\boldsymbol{c}$ is arbitrary [14]. Now eq. (2.5) can be rewritten as:

$$\underbrace{\left(\int_{\Omega} \boldsymbol{B}^T \boldsymbol{D} \boldsymbol{B}\ d\Omega\right)}_{\boldsymbol{K}} \boldsymbol{a} = \int_{\Gamma_\sigma} \boldsymbol{N}^T\ \boldsymbol{t}\ d\Gamma + \int_{\Omega} \boldsymbol{N}^T\ \boldsymbol{b}\ d\Omega = \boldsymbol{f} \tag{2.8}$$

$$\boldsymbol{K}\ \boldsymbol{a} = \boldsymbol{f} \qquad \Leftrightarrow \qquad \boldsymbol{f_{internal}} = \boldsymbol{f_{external}} \tag{2.9}$$

Here, $\boldsymbol{K}$ is the global stiffness matrix and $\boldsymbol{f}$ is the nodal forces. The displacement vector $\boldsymbol{a}$ can be split up into two parts, $\boldsymbol{a_f}$ and $\boldsymbol{a_c}$ where $\boldsymbol{a_f}$ is the displacement of the free nodes and $\boldsymbol{a_c}$ is the displacement of the constrained nodes.

$$\boldsymbol{a_f} = \begin{bmatrix} a_1 & a_2 & \cdots & a_{nfree} \end{bmatrix}^T \qquad \boldsymbol{a_c} = \begin{bmatrix} a_{nfree+1} & \cdots & a_{ndofs} \end{bmatrix}^T$$

Here, $\boldsymbol{a_c}$ is prescribed and thus known and $\boldsymbol{a_f}$ is the actual unknowns. The same split can be introduced for the shape functions and for the internal and external force vectors. The displacement $\boldsymbol{u}$ can then be approximated as $\boldsymbol{u} \approx \boldsymbol{N_f a_f} + \boldsymbol{N_c a_c}$ and the splitting of force vectors gives two equations:

$$\boldsymbol{f_{int}} = \begin{bmatrix} \boldsymbol{f_{int,f}(a)} \\ \boldsymbol{f_{int,c}(a)} \end{bmatrix} = \begin{bmatrix} \boldsymbol{f_{ext,f}(a)} \\ \boldsymbol{f_{ext,c}(a)} \end{bmatrix} = \boldsymbol{f_{ext}} \tag{2.10}$$

From the first row of eq. (2.10), one can obtain:

$$\boldsymbol{f_{int,f}} \begin{pmatrix} \boldsymbol{a_f} \\ \boldsymbol{a_c} \end{pmatrix} = \underbrace{\int_{\Gamma_\sigma} \boldsymbol{N_f^T}\ \boldsymbol{t}\ d\boldsymbol{\Gamma_\sigma} + \int_{\Omega} \boldsymbol{N_f^T}\ \boldsymbol{b}\ d\boldsymbol{\Omega}}_{\boldsymbol{f_{ext,f}}} \tag{2.11}$$

In a more concise format, the system of eq. (2.11) can be rewritten as follows:

$$\boldsymbol{g(a_f)} = \boldsymbol{f_{int,f}} \begin{pmatrix} \boldsymbol{a_f} \\ \boldsymbol{a_c} \end{pmatrix} - \boldsymbol{f_{ext,f}} = \boldsymbol{0} \tag{2.12}$$

The vector $\boldsymbol{g}$ in eq. (2.12) is called *out-of-balance force vector*. For nonlinear problems $\boldsymbol{a_f}$ can not be solved explicitly. In order to solve eq. (2.12) for $\boldsymbol{a_f}$, it is necessary to implement an iteration technique, typically Newton's method, described below, until convergence is reached. The solution $\boldsymbol{a_f}$ can then be used in $\boldsymbol{f_{int,c}(a)} = \boldsymbol{f_{ext,c}}$ to calculate the reaction forces on the prescribed boundary.

2.2 Iterative solution technique - Newton's method

As it was mentioned in the previous section, the displacements of the free nodes, $\boldsymbol{a_f}$ can not be solved explicitly for nonlinear problems. One of the most common solution technique used in FEA is the Newton's iteration method which uses the first order derivative of the out-of-balance force vector $\boldsymbol{g}$, known as the jacobian matrix $\boldsymbol{J}$, to solve the nonlinear equilibrium equations.

$$\boldsymbol{J} = \frac{\mathrm{d}\boldsymbol{g}}{\mathrm{d}\boldsymbol{x}} = \begin{bmatrix} \frac{\partial g_1}{\partial x_1} & \frac{\partial g_1}{\partial x_2} & \cdots & \frac{\partial g_1}{\partial x_{nfree}} \\ \frac{\partial g_2}{\partial x_1} & \frac{\partial g_2}{\partial x_2} & \cdots & \frac{\partial g_2}{\partial x_{nfree}} \\ \vdots & \vdots & \ddots & \vdots \\ \frac{\partial g_{nfree}}{\partial x_1} & \frac{\partial g_{nfree}}{\partial x_2} & \cdots & \frac{\partial g_{nfree}}{\partial x_{nfree}} \end{bmatrix} \tag{2.13}$$

Here, $\boldsymbol{x} = \boldsymbol{a_f}$. It should be noted that the jacobian depends on the vector $\boldsymbol{x}$, hence $\boldsymbol{J} = \boldsymbol{J(x)}$. Now, let assume that $\boldsymbol{x}^{(k)}$ is an initial estimate of the solution. Linearization of the equations $\boldsymbol{g(x^{(k)}) = 0}$ around this point gives the Taylor series approximation:

$$\boldsymbol{g}(\boldsymbol{x}^{(k)} + \Delta\boldsymbol{x}) = \boldsymbol{g}(\boldsymbol{x}^{(k)}) + \boldsymbol{J}(\boldsymbol{x}^{(k)})\Delta\boldsymbol{x} + O((\Delta\boldsymbol{x})^2) \approx \boldsymbol{g}(\boldsymbol{x}^{(k)}) + \boldsymbol{J}(\boldsymbol{x}^{(k)})\Delta\boldsymbol{x} \tag{2.14}$$

The linear equations $\boldsymbol{g}(\boldsymbol{x}^{(k)} + \Delta\boldsymbol{x}) = \boldsymbol{0}$ can be solved for $\Delta\boldsymbol{x}$. This "correction", $\Delta\boldsymbol{x}$, is then added to the previous solution value to calculate a better estimation $\boldsymbol{x}^{(k+1)}$.

$$\begin{aligned} \Delta\boldsymbol{x}^{(k)} &= -\boldsymbol{J}(\boldsymbol{x}^{(k)})^{-1}\boldsymbol{g}(\boldsymbol{x}^{(k)}) \\ \boldsymbol{x}^{(k+1)} &= \boldsymbol{x}^{(k)} + \Delta\boldsymbol{x}^{(k)} \end{aligned} \tag{2.15}$$

For each iteration, the solution will be updated until it converges.

2.3 Elements

Different types of solid elements can be used in Abaqus for FEM simulations e.g. tetrahedral (tet) and hexahedral (brick) elements, see fig. 2.3. Both element types are available as first (linear) and second (quadratic) order approximations.

2.3.1 Tetrahedral elements

The tetrahedral element has the benefit of being easy meshed, that is, a geometry can be meshed with less effort as compared with the hexahedral element. This is why many automatic meshing algorithms uses the tet element. The drawback is that when using tets, the model will become overly stiff and slow converging, meaning that a very fine mesh is required to produce a satisfying result. This is why tets should be avoided and if used, only in noncritical areas.

It is well known that linear tetrahedral elements perform poorly in problems with plasticity, nearly incompressible materials, and pure bending. For a variety of reasons, low-order tetrahedral elements are preferable to quadratic tetrahedral elements, particularly for nonlinear problems. Second-order tetrahedral are not suitable for the analysis of contact problems. A constant pressure on an element face produces zero equivalent loads at the corner nodes. In contact problems this makes the contact condition at the corners indeterminate, with failure of the solution likely because of excessive gap chatter. The same argument holds true for contact on triangular faces of a wedge element [16].

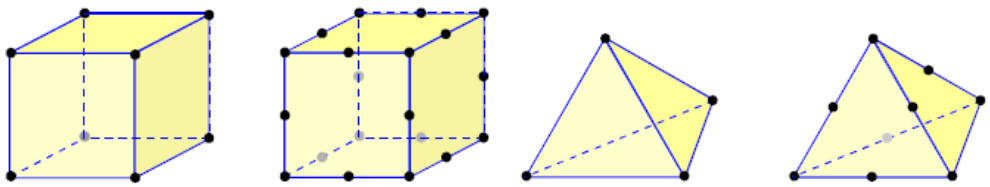

(a) *Hexahedral.* (b) *Tetrahedral.*

Figure 2.3: *Linear and quadratic hexahedral and tetrahedral elements.*

2.3.2 Hexahedral elements

A hexahedral element is topologically equivalent to a cube. It has eight corners, twelve edges and six faces. Finite elements with this geometry are extensively used in modeling three-dimensional solids due to its property of giving the best results for the minimum cost. The natural coordinates for a hexahedral element are called ξ, η and μ, and are called isoparametric hexahedral coordinates or natural coordinates, see fig. 2.4. The natural coordinates vary from -1 to +1 over the element face. The eight corners of the element are locally numbered 1, 2, ..., 8. In order to guarantee a positive volume or more precisely, a positive jacobian determinant at every point, the corners are numbered by following rules:

1. Chose one starting corner, which is given number 1 and one initial face pertaining to that corner.
2. Number the other 3 corners as 2, 3, 4 traversing the initial face counter-clockwise while one looks at the initial face from the opposite one.
3. Number the corners of the opposite face directly opposite 1, 2, 3, 4 as 5, 6, 7, 8, respectively.

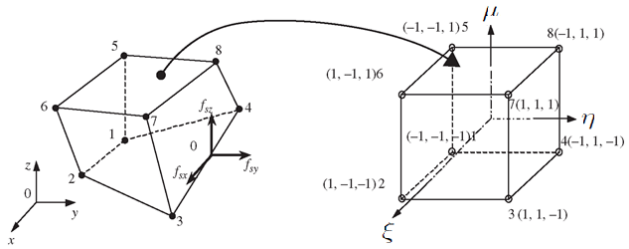

Figure 2.4: *The 8-nodal hexahedral transformation between coordinate systems.*

The simplest hexahedral element is the eight-nodal hexahedral (linear hexahedron element). For a 3D elasticity problem, each node has 3 translational degrees of freedom (DOF), making a total of 24 DOF's in a hexahedron element. The element shape functions of linear hexahedron element are given in the local natural coordinate system as:

$$N_1^e = \frac{1}{8}(1-\xi)(1-\eta)(1-\mu), \qquad N_2^e = \frac{1}{8}(1+\xi)(1-\eta)(1-\mu)$$
$$N_3^e = \frac{1}{8}(1+\xi)(1+\eta)(1-\mu), \qquad N_4^e = \frac{1}{8}(1-\xi)(1+\eta)(1-\mu)$$
$$N_5^e = \frac{1}{8}(1-\xi)(1-\eta)(1+\mu), \qquad N_6^e = \frac{1}{8}(1+\xi)(1-\eta)(1+\mu)$$
$$N_7^e = \frac{1}{8}(1+\xi)(1+\eta)(1+\mu), \qquad N_8^e = \frac{1}{8}(1-\xi)(1+\eta)(1+\mu)$$

where the isoparametric hexahedron coordinates ξ, η and μ for each node are:

Node	ξ	η	μ
1	-1	-1	-1
2	1	-1	-1
3	1	1	-1
4	-1	1	-1
5	-1	-1	1
6	1	-1	1
7	1	1	1
8	-1	1	1

2.3.3 Element Matrices

Since the shape functions are defined in terms of the natural coordinates, to obtain the derivatives of the shape functions with respect to cartesian coordinates x, y and z, the chain rule of partial differentiation needs to be used. The derivatives can be written in matrix form as:

$$\begin{bmatrix} \frac{\partial N_i^e}{\partial x} \\ \frac{\partial N_i^e}{\partial y} \\ \frac{\partial N_i^e}{\partial z} \end{bmatrix} = \begin{bmatrix} \frac{\partial \xi}{\partial x} & \frac{\partial \eta}{\partial x} & \frac{\partial \mu}{\partial x} \\ \frac{\partial \xi}{\partial y} & \frac{\partial \eta}{\partial y} & \frac{\partial \mu}{\partial y} \\ \frac{\partial \xi}{\partial z} & \frac{\partial \eta}{\partial z} & \frac{\partial \mu}{\partial z} \end{bmatrix} \begin{bmatrix} \frac{\partial N_i^e}{\partial \xi} \\ \frac{\partial N_i^e}{\partial \eta} \\ \frac{\partial N_i^e}{\partial \mu} \end{bmatrix} \tag{2.16}$$

The 3×3 matrix that appears in the equation above is the inverse of the jacobian matrix $\boldsymbol{J}$ of (x, y, z) with respect to (ξ, η, μ). The equation above can then be used to compute the strain matrix $\boldsymbol{B}$ which is defined as:

$$\boldsymbol{B}^e = \begin{bmatrix} \frac{\partial}{\partial x} & 0 & 0 \\ 0 & \frac{\partial}{\partial y} & 0 \\ 0 & 0 & \frac{\partial}{\partial z} \\ 0 & \frac{\partial}{\partial z} & \frac{\partial}{\partial y} \\ \frac{\partial}{\partial z} & 0 & \frac{\partial}{\partial x} \\ \frac{\partial}{\partial y} & \frac{\partial}{\partial x} & 0 \end{bmatrix} \begin{bmatrix} \boldsymbol{q} & \boldsymbol{0} & \boldsymbol{0} \\ \boldsymbol{0} & \boldsymbol{q} & \boldsymbol{0} \\ \boldsymbol{0} & \boldsymbol{0} & \boldsymbol{q} \end{bmatrix} \tag{2.17}$$

where $\boldsymbol{q} = [N_1^e, \ \ldots, \ N_8^e]$. Once the strain matrix $\boldsymbol{B}$ is computed, the element stiffness matrix can be obtained by

$$\boldsymbol{K}^e = \int_{V^e} \boldsymbol{B}^T \boldsymbol{D} \boldsymbol{B} dV \tag{2.18}$$

The material properties are defined by the constitutive matrix $\boldsymbol{D}$. The integral in eq. (2.18) is evaluated using numerical integration, most commonly Gauss integration, which involves a triple loop over conventional Gauss quadrature points. Assuming that the constitutive matrix $\boldsymbol{D}$ is constant over the element, the element stiffness matrix can be rewritten as:

$$\boldsymbol{K}^e = \sum_{i=1}^{p_1} \sum_{j=1}^{p_2} \sum_{k=1}^{p_3} w_i w_j w_k \boldsymbol{B}_{ijk}^T \boldsymbol{D} \boldsymbol{B}_{ijk} J_{ijk} \tag{2.19}$$

Here w_1, w_2, w_3 are the Gauss point weights in each direction and p_1, p_2 and p_3 are the number of Gauss points in the ξ, η and μ direction, respectively. Usually the number of integration points is taken the same in all directions, thus the total number of Gauss points is p^3. Using n Gauss points in one direction will integrate an function of order $2n-1$ exactly, using less points is called a reduced integration. $\boldsymbol{B}_{ijk}$ and J_{ijk} are abbreviations for:

$$\boldsymbol{B}_{ijk} = \boldsymbol{B}(\xi_i, \eta_j, \mu_k), \qquad J_{ijk} = \det \boldsymbol{J}(\xi_i, \eta_j, \mu_k) \tag{2.20}$$

In Abaqus, the linear hexahedral element is denoted C3D8 and C3D8R. Abaqus uses two integration points in each direction, eight in total, for the C3D8 element and one point for the C3D8R element (reduced integration).

2.3.4 Shear locking and hourglassing

Two numerical problems seldom discussed in academic finite element textbooks like Ottosen and Petersson [14] are shear locking and hourglassing [17]. It is therefore necessary for the engineer to have a solid understanding of how major commercial FEA codes handle these difficulties when analysing the results.

Shear locking is a result of the first order brick not being able to replicate pure bending properly. From beam theory it is known that the normal of a cross section will stay parallel to the beam axis and no shear stresses exist when a pure bending condition is applied. When the linear brick element is subjected to the same condition, the end faces will bend but the top surfaces will stay flat due to the linear shape functions, as illustrated in fig. 2.5. This will result in artificial shear stresses making the element appear overly stiff. To minimize the error it is recommended to use reduced integration, described below and have a number of elements through the thickness. It should be noted that second order bricks do not exhibit the shear locking problem, although they increase computational time.

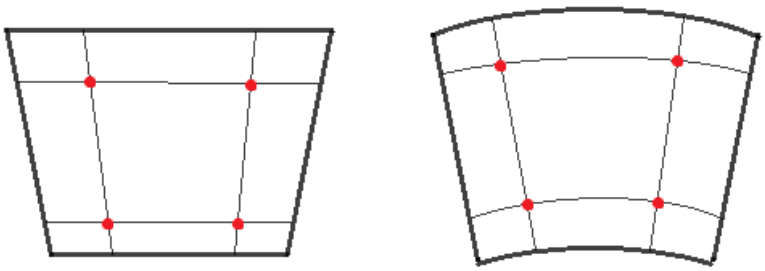

Figure 2.5: *Comparison between a fully integrated linear element and a ideal solid in bending, integration points marked in red.*

The shear locking phenomenon can be cured by using reduced integration. Instead of using 2 integration points in each direction, making a total of 8 points for the fully integrated linear brick, only one point is used for the reduced integration brick. But this method exhibits another flaw, known as hourglassing. Since the stresses and strains are evaluated at the integration point, having only one centre integration point will result in spurious energy modes since the element can deform without the centre point experiencing strain, as seen in fig. 2.6. Abaqus uses an hourglass control scheme to minimize this error.

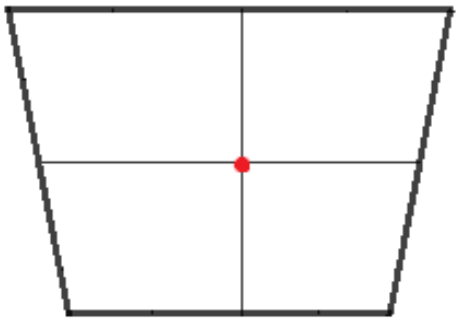

Figure 2.6: *Reduced integration brick suffering from "hourglassing".*

2.4 Material Model

Initially, most materials of engineering interest respond elastically. Elastic behaviour means that the deformation is fully recoverable when the load is removed i.e. the specimen returns to its original shape. If the load exceeds some limit (denoted yield limit, σ_y), the deformation is no longer fully recoverable. Some part of the deformation, denoted ϵ^p, will remain when the load is removed which means that the material has deformed plastically. There are two broad groups of metal plasticity problem which are of interest to the engineer and analyst.

The first group involves relatively small plastic strains, often of the same order as the elastic strains which occur. Analysis of problems involving small plastic strains allows one to design structures optimally, assuring they will not fail when in service and at the same time are not stronger than they really need to be. In this sense, plasticity is seen as a material failure. The second group of problems involves very large strains and deformations. These problems occurs in analysis of metal manufacturing and forming processes, which can involve extrusion, drawing, forging, rolling and so on. The analyses in this project involve small plastic strains. The material models used to perform the analyses are *elastoplastic*.

2.4.1 Elastoplastic material model

An elastoplastic material model is commonly used for metal plasticity, either as a rate-dependent or as a rate-independent model. The simplest type of plasticity model is an isotropic, perfectly elastoplastic material with an associated flow rule. The stress-strain relationship of this type of material model is shown in fig. 2.7.

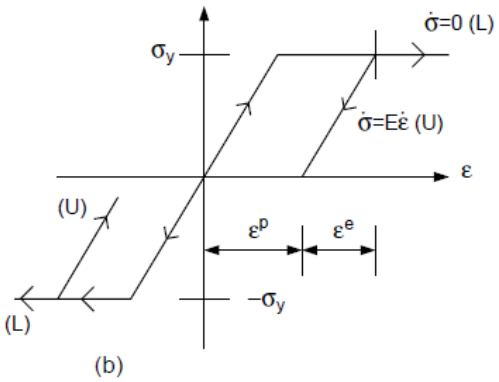

Figure 2.7: *Stress-strain relationship for perfectly elastoplastic material model.*

The free energy is expressed as

$$\Psi = \frac{1}{2}E(\epsilon)^2 = \frac{1}{2}E(\epsilon - \epsilon^P)^2 \tag{2.21}$$

where ϵ^e is the elastic strain, ϵ^P is the plastic strain, ϵ is the total strain and E is the modulus of elasticity. The constitutive equation for the stress is obtained as

$$\sigma = \frac{\partial \Psi}{\partial \epsilon} = E(\epsilon - \epsilon^P) \tag{2.22}$$

and for the dissipative stress

$$\sigma^P = -\frac{\partial \Psi}{\partial \epsilon^P} = E(\epsilon - \epsilon^P) = \sigma \tag{2.23}$$

The yield criterion is $\Phi = 0$, where Φ is chosen as

$$\Phi(\sigma) = |\sigma| - \sigma_y \tag{2.24}$$

The material response is elastic when $|\sigma| < \sigma_y$, but when $\Phi = 0$ plastic strain will be produced. The constitutive rate equation for ϵ^P is then postulated as the *associative flow rule*:

$$\dot{\epsilon}^P = \lambda \frac{\partial \Phi}{\partial \sigma} = \lambda \frac{\sigma}{|\sigma|} \tag{2.25}$$

where λ is the plastic multiplier, a positive scalar variable. By combining eq. (2.25) and eq. (2.23), the differential equation for the stress is obtained as

$$\dot{\sigma} = E\dot{\epsilon} - \lambda E \frac{\sigma}{|\sigma|} \tag{2.26}$$

The problem formulation is complemented by the *elastoplastic loading criteria*

$$\lambda \geq 0, \quad \Phi(\sigma) \leq 0, \quad \lambda\ \phi(\sigma) = 0 \tag{2.27}$$

Hardening plasticity

A perfectly elastoplastic material subjected to uniaxial loading yields at a constant stress. During plastic flow under general multiaxial loading, the stress state can move along the yield surface, but the surface itself remains unchanged. However, in reality the microstructure of the material changes as plastic flow continues, and this causes a change of the properties observable on the macroscale. Under uniaxial loading, the stress transmitted by a yielding material can increase or decrease. An increase of the yield stress is referred to as *hardening* [18]. The stress-strain relationship for a material that hardens linearly can be seen in fig. 2.8.

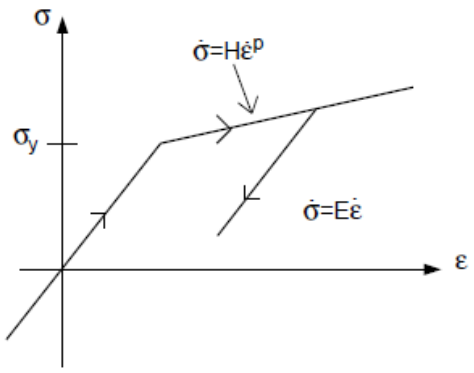

Figure 2.8: *Stress-strain relationship for a hardening material.*

When modelling the hardening using a kinematic hardening assumption, the increase of the yield limit is described by the hardening modulus H which is related to the plastic strain. Upon unloading and reloading, the plasticity will occur again when $|\sigma| > \sigma_y + H|\epsilon^P|$. The energy density for this type of material is expressed as

$$\Psi = \frac{1}{2}E(\epsilon - \epsilon^P)^2 + \frac{1}{2}Hk^2 \tag{2.28}$$

where k is the hardening variable. The constitutive equation for stress and the dissipative stress κ, associated with k, are given as

$$\sigma = \frac{\partial \Psi}{\partial \epsilon} = E(\epsilon - \epsilon^P) \tag{2.29}$$

$$\sigma^P = -\frac{\partial \Psi}{\partial \epsilon^P} = \sigma \tag{2.30}$$

$$\kappa = -\frac{\partial \Psi}{\partial k} = -Hk \tag{2.31}$$

The yield function is then defined as

$$\Phi(\sigma, \kappa) = |\sigma| - \sigma_y - \kappa \tag{2.32}$$

Plastic strain will be produced when $\Phi = 0$. The associative flow and hardening rules are then defined as

$$\dot{\epsilon}^P = \lambda \frac{\partial \Phi}{\partial \sigma} = \lambda \frac{\sigma}{|\sigma|} \tag{2.33}$$

$$\dot{k} = \lambda \frac{\partial \Phi}{\partial \kappa} = -\lambda \tag{2.34}$$

where the plastic multiplier λ is still defined by eq. (2.27). Combining eq. (2.33) and (2.29) gives the differential equation for the stress. A rate equation for κ can also be obtained by differentiating eq. (2.31) and combining with eq. (2.34) as

$$\begin{aligned} \dot{\sigma} &= E\dot{\epsilon} - \lambda E \frac{\sigma}{|\sigma|} \\ \dot{\kappa} &= H\lambda \end{aligned} \tag{2.35}$$

Thus, the loading criteria is defined as

$$\lambda \geq 0, \quad \Phi(\sigma, \kappa) \leq 0, \quad \lambda\phi(\sigma, \kappa) = 0 \tag{2.36}$$

2.5 Contact theory

Contact interactions between different parts play a key role when simulating bolted assemblies, manufacturing processes, dynamic impact events, and various other systems. There are several methods that offer the desired solutions to a body contact problems. The most commonly used methods for contact analysis are *the penalty method* and *the Lagrange multiplier method*. The main difference between them is the way they include the potential energy of contacting surfaces in their formulation. Each of the methods has its advantages and disadvantages.

The advantage of the penalty method is that the contact constraints are taken into account with no increase in the number of DOF, but this leads to non-physical penetration, while the Lagrange multiplier method introduces additional DOFs in the system, but does fulfil the constraint equation correctly. In order to understand the basic methodology and difficulties related to contact mechanics, a simple contact problem will be discussed.

Consider a contact problem consisting of a point mass m under gravitational load which is supported by a spring with stiffness k, see fig. 2.9. The energy for this system can be written as:

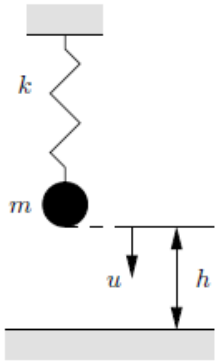

Figure 2.9: *Point mass supported by a spring.*

$$\Pi(u) = \frac{1}{2}ku^2 - mgu \tag{2.37}$$

The extremum of eq. (2.37) can be computed by variation as:

$$\delta\Pi(u) = ku\delta u - mg\delta u = 0 \tag{2.38}$$

The extremum of eq. (2.37) is a minumum at $u = \frac{mg}{k}$, since the second variation of Π is $\delta^2\Pi = k$. Due to the rigid support below the mass, the motion of the mass is restricted. The restriction of the motion can be described by the *gap function* $c(u)$:

$$c(u) = h - u \geq 0 \tag{2.39}$$

which excludes penetration as an inequality constraint. For $c(u) > 0$, there exists a gap between the point mass and the rigid support and for $c(u) = 0$ this gap is closed. From linearisation of eq. (2.39) around $u = h$, one can obtain $\delta u \leq 0$, which means that the virtual displacement has to fulfil the constraint and can only point in the upward direction. Using this in eq. (2.38) leads to a *variational inequality*

$$ku\delta u - mg\delta u \geq 0 \tag{2.40}$$

Due to the restriction of the solution space by the constraint condition, the solution of eq. (2.37) is not the minimum point associated with Π_{min}, but at the point associated with Π^c_{min}, which denotes the minimal energy within the admissible solution space, see fig. 2.10.

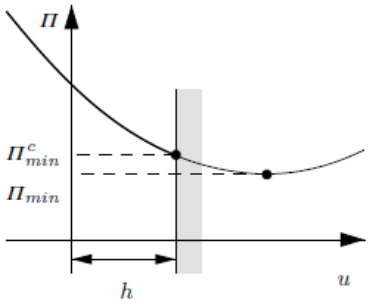

Figure 2.10: *Energy of the mass spring.*

Instead of the variation δu, one can use the difference between the a test function v and the solution u, i.e. $\delta u = v - u$. The test function must just like the solution u fulfil the condition $v - h \leq 0$ at the contact point. By inserting $\delta u = v - u$ in eq. (2.38), one obtains

$$ku(v - u) - mg(v - u) = 0 \tag{2.41}$$

Since the force mg is greater than the spring force ku at the contact point, using the constraint equation $v - h \leq 0$ will give the inequality

$$ku(v - h) \geq mg(v - h) \tag{2.42}$$

Once the point mass contacts the rigid surface, a reaction force f_R appears. Assuming that the reaction force between the rigid surface and the point mass is negative, the contact pressure can only be compression. Such assumption leads to the restriction $R_N \leq 0$. This means that two cases within a contact problem where the motion is constrained exist, compression state in which the conditions $c(u) = 0$ and $R_N < 0$ are valid or that the spring stiffness is sufficiently large enough to prevent any contact between the point mass and the rigid surface. In this case conditions $c(u) > 0$ and $R_N = 0$ are valid. both cases can be combined in the statement

$$c(u) \geq 0, \qquad R_N \leq 0 \text{ and } R_N c(u) = 0 \tag{2.43}$$

2.5.1 Lagrange multiplier method

By assuming that the conditions $c(u) = 0$ and $R_N < 0$ are fulfilled by the solution, i.e. the point mass comes into contact with the rigid support, the Lagrange multiplier method adds to the energy of the system eq. (2.37) a term which contains the constraint:

$$\Pi(u, \lambda) = \frac{1}{2}ku^2 - mgu + \lambda c(u) \tag{2.44}$$

The variation of eq. (2.44) leads to two equations, since δu and $\delta\lambda$ can be varied independently.

$$\begin{aligned} ku\delta u - mg\delta u - \lambda\delta u &= 0 \\ c(u)\delta\lambda &= 0 \end{aligned} \tag{2.45}$$

The first equation represents the equilibrium for the point mass including the reaction force when it touches the rigid surface and the second equation is the fulfilment of the kinematic constraint equation for the contact, i.e. $u = h$. Due to that, the variation is no longer restricted and the Lagrange multiplier λ which is equivalent with the reaction force R_N can be solved:

$$\lambda = kh - mg = R_N \tag{2.46}$$

The condition $R_N \leq 0$ still has to be fulfilled by the solution eq. (2.46). If the condition is not met, then the assumption of the contact no longer holds. This means that constraint is inactive, i.e. there is no contact between the mass point and the rigid surface and the correct solution is computed from eq. (2.38).

2.5.2 Penalty method

Another widely used method to solve contact problems is the penalty method. This is because only the primary displacement variables enter the formulation. Here, for an active constraint, i.e. when there is contact between the mass point and the rigid surface, a penalty term is added to the energy of the system eq. (2.37):

$$\Pi(u) = \frac{1}{2}ku^2 - mgu + \frac{1}{2}\epsilon[c(u)]^2 \qquad \text{with } \epsilon > 0 \tag{2.47}$$

the penalty parameter can be interpreted as a spring stiffness in the contact interface between the point mass and the rigid support, see fig. 2.11. This is because the energy of the penalty term has the same structure as the potential energy of a simple spring. The variation of eq. (2.47) is computed as:

$$ku\delta u - mg\delta u - \epsilon c(u)\delta u = 0 \tag{2.48}$$

From eq. (2.48), one can derive the solution

$$u = \frac{mg + \epsilon h}{k + \epsilon} \tag{2.49}$$

The value of the constraint equation then becomes:

$$c(u) = h - u = \frac{kh - mg}{k + \epsilon} \tag{2.50}$$

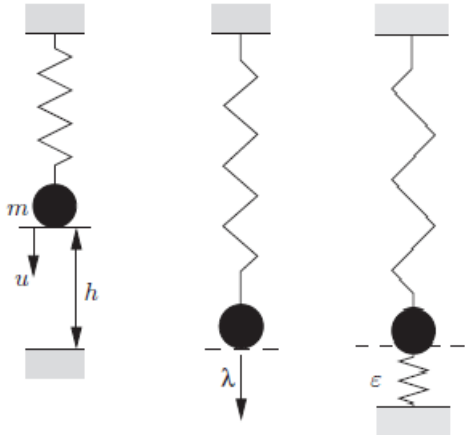

Figure 2.11: *Point mass supported by a spring, free body diagram for the Lagrange multiplier method and a penalty spring due to the penalty term.*

During contact, $mg \geq kh$ which means that a penetration of the point mass into the rigid support occurs. Physically, it is equivalent to a compression of the spring. It should be noted that the penetration depends on the penalty parameter. In order to fulfil the constraint equation eq. (2.39), the penalty term is in the limit $\epsilon \to \infty \implies c(u) \to 0$. Hence, in the penalty method, two limiting cases can be distinguished:

1. $\epsilon \to \infty \Longrightarrow u - h \to 0$, which means that ones approaches the correct solution for very large penalty parameters.
2. $\epsilon \to 0$ represents the unconstrained solution and is only valid for inactive constraints.

The reaction force in penalty method is computed from $R_N = \epsilon c(u)$. In this case, it is equal to

$$R_N = \lambda = \epsilon c(u) = \frac{\epsilon}{k+\epsilon}(kh - mg) \tag{2.51}$$

which in the limit $\epsilon \to \infty$ yields the correct solution obtained with the Lagrange multiplier method, eq. (2.46).

2.6 Fatigue life

Components of machines, vehicles and structures are frequently subjected to cyclic loads, and the resulting cyclic stresses can lead to microscopic physical damage to the materials involved. Even at stresses below a given material's yield limit, this microscopic damage can accumulate with continued cycling until it develops into a crack or other microscopic damage that leads to failure of the component. This process of damage and failure due to cyclic loading is called *fatigue*. Fatigue life is defined as the number of load cycles that a structure sustains before failure [19].

Currently, there are three different approaches to analysing and designing against fatigue failure, *stress-based approach* or *high cycle fatigue* which is based on the nominal stresses in the affected region of the component, *strain-based approach* or *low cycle fatigue* which involves more detailed analysis of the local yielding and *fracture mechanics approach* which treats growing cracks by the method of fracture mechanics. In this project only high cycle fatigue is considered, the reason for this is described in section 3.4.

2.6.1 High cycle fatigue

High cycle fatigue (HCF) focuses on situations that require more than 10^4 cycles to failure where the stress is sufficiently low and deformation is primarily elastic, i.e. yielding effects will not dominate the behaviour. In HFC, the number of cycles to failure is characterized by *stress-life* curves, also called an *S-N* curves. In such a curve, the stresses are usually plotted as stress amplitudes, σ_a, versus the number of cycles to failure, N_f, which changes rapidly with stress level. For this reason, the cycle numbers are usually plotted in a logarithmic scale.

The *S-N* curves most commonly available are obtained from bending or axial tests, which involve a uniaxial state of stress, but the state of stress in notches is usually multiaxial and not the same as the state of stress in the main body. In order to be able to predict the fatigue life of components that involve multiaxial state of stress, it is necessary to apply the data from uniaxial behaviour and tests to multiaxial situations by choosing among many various multiaxial effective stress methods such as Dang Van, Signed von Mises, Crossland, Manson-McKnight etc.

2.6.2 Multiaxial fatigue

Multiaxial loading can be divided into two groups, proportional loading (in-phase) and nonproportional loading (out-of-phase). During proportional loading the principal stress directions remain fixed in time while in nonproportional loading the directions of the principal stresses change in time which make the fatigue life prediction more complicated. In this project, the fatigue life of the components will be predicted when the flanges are subjected only to the proportional loading, consisting of a fluctuating bending moment.

The state of stress and strain at a point in the body can be described by six stress components ($\sigma_x, \sigma_y, \sigma_z, \sigma_{xy}, \sigma_{xz}, \sigma_{yz}$) and six strain components ($\epsilon_x, \epsilon_y, \epsilon_z, \epsilon_{xy}, \epsilon_{xz}, \epsilon_{yz}$) acting on orthogonal planes x, y and z. Stresses and strains acting in any other direction or plane can be found by using transformation equations. These stress components are used to evaluate a equivalent stress that can be compared with the fatigue limit of standard *S-N* curves. The two methods used for fatigue analysis in this project are presented below.

Signed von Mises method

The equivalent von Mises stress is defined as:

$$\sigma_{eq,vM} = \sqrt{\frac{1}{2}\Big((\sigma_x - \sigma_y)^2 + (\sigma_y - \sigma_z)^2 + (\sigma_z - \sigma_x)^2 + 6\ (\sigma_{xy}^2 + \sigma_{yz}^2 + \sigma_{zx}^2)\Big)} \tag{2.52}$$

The signed von Mises method analyses the equivalent stress signed by the sign of the first stress tensor invariant, I_1 during loading. The first stress tensor invariant is defined as $I_1 = \sigma_x + \sigma_y + \sigma_z$. The maxima and the minima

of the current signed von Mises stress during loading serve to define the amplitude and the mean stress:

$$\begin{aligned}\sigma_a &= \frac{\max\limits_t \left[\sigma_{eq,vM}\ \mathrm{sign}(I_1)\right] - \min\limits_t \left[\sigma_{eq,vM}\ \mathrm{sign}(I_1)\right]}{2} \\ \sigma_m &= \frac{\max\limits_t \left[\sigma_{eq,vM}\ \mathrm{sign}(I_1)\right] + \min\limits_t \left[\sigma_{eq,vM}\ \mathrm{sign}(I_1)\right]}{2}\end{aligned} \tag{2.53}$$

With these two values, one can estimate the fatigue life from a *S-N* curve or apply a method of predicting life from given uniaxial mean and alternating stresses [20].

Manson-McKnight method

The Manson-Mcknight method is based on von Mises hypothesis and is aimed to reduce the multiaxial stress state to an equivalent uniaxial stress. In this approach, the amplitude and mean stresses are computed from the maxima and minima of every stress tensor component during the loading cycle:

$$\begin{aligned}\sigma_{i,a} &= \frac{\max\limits_t (\sigma_i) - \min\limits_t (\sigma_i)}{2} \qquad && i = x, y, z \\ \sigma_{ij,a} &= \frac{\max\limits_t (\sigma_{ij}) - \min\limits_t (\sigma_{ij})}{2} \qquad && ij = xy, yz, xz \\ \sigma_{i,m} &= \frac{\max\limits_t (\sigma_i) + \min\limits_t (\sigma_i)}{2} \qquad && i = x, y, z \\ \sigma_{ij,m} &= \frac{\max\limits_t (\sigma_{ij}) + \min\limits_t (\sigma_{ij})}{2} \qquad && ij = xy, yz, xz\end{aligned} \tag{2.54}$$

The corresponding equivalent amplitude and mean stresses that represent the uniaxial stress state are defined as:

$$\begin{aligned}\sigma_a &= \sqrt{\frac{1}{2}\left((\sigma_{x,a} - \sigma_{y,a})^2 + (\sigma_{y,a} - \sigma_{z,a})^2 + (\sigma_{z,a} - \sigma_{x,a})^2 + 6\ (\sigma_{xy,a}^2 + \sigma_{yz,a}^2 + \sigma_{zx,a}^2)\right)} \\ \sigma_m &= B\ \sqrt{\frac{1}{2}\left((\sigma_{x,m} - \sigma_{y,m})^2 + (\sigma_{y,m} - \sigma_{z,m})^2 + (\sigma_{z,m} - \sigma_{x,m})^2 + 6\ (\sigma_{xy,m}^2 + \sigma_{yz,m}^2 + \sigma_{zx,m}^2)\right)}\end{aligned} \tag{2.55}$$

where $B = \mathrm{sign}\ (I_{1,d})$. Here $I_{1,d}$ is the value of the first stress tensor invariant at the moment when it reaches the greatest distance from zero during the loading [20]. With σ_a and σ_m, one can predict the fatigue life of the component of interest from a *S-N* curve.

3 Methodology

The methodology chapter is divided into two sections. The first section describes how the model was implemented in the software. It includes presentation of the geometries, material models, interaction properties, submodelling and finite element discretization. The subsequent section describes the criteria used when evaluating the capacities as well as how the fatigue assessment was conducted.

3.1 Geometries

The flange assemblies consisted of two flanges, a TX titanium alloy seal and assembly bolts, seen in fig. 3.1. The seal is placed in the hollow space between the flanges to improve the leakage capacity. The bolt holes on the lower flange are threaded and the bolts are joined to the flange by the threads on the lower part of the bolts. The separate parts are presented further in the following sections.

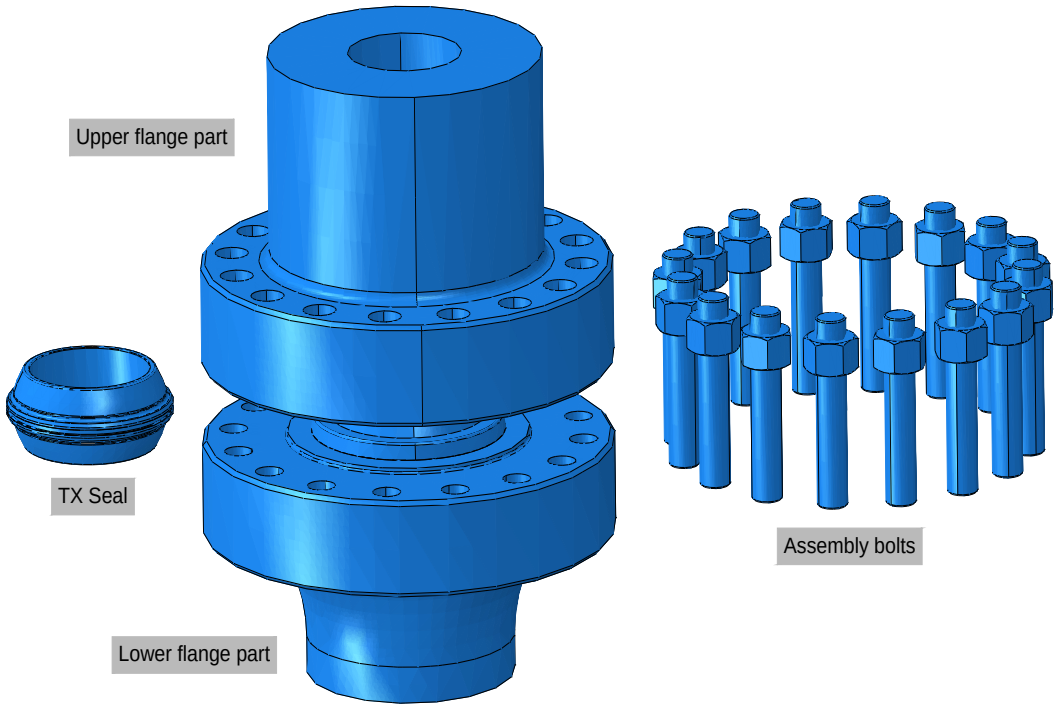

Figure 3.1: *The assembly, consisting of the TX seal, the flanges and the bolts.*

3.1.1 Flanges

The flanges consist of a pipe with a bore diameter of 7 3/8 in. The lower flange has a larger radius and a smaller pipe wall thickness as compared with the upper flange. The material used was 80 KSI steel, with properties presented in table 3.2.

The difference between the flange assemblies is seen in fig. 3.2, where the lower part of the raised face flange has a raised circular area on the hub face. The flat hub face flange, has a larger contact area, consisting of the entire area from the inner hub radius to the outer hub radius. The raised face flange has a separation between the hub faces, resulting in a smaller contact area and thus a higher hub face contact pressure when loaded in compression.

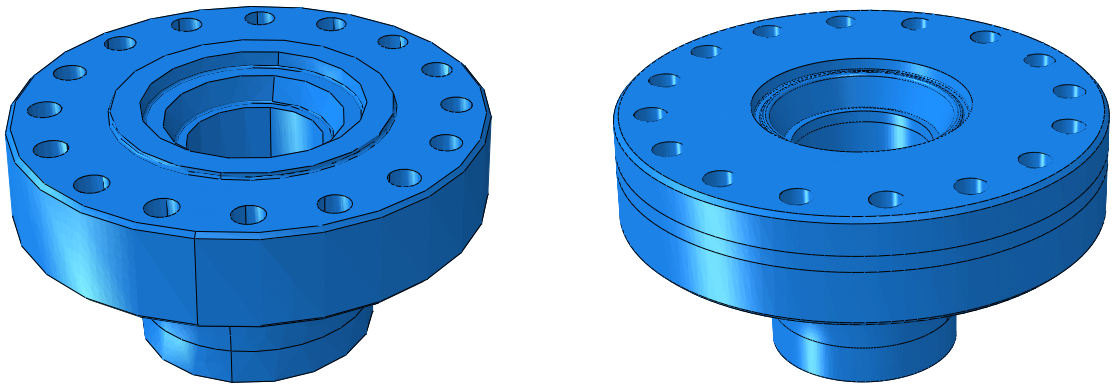

(a) *Lower flange with raised face.* (b) *Lower flange with flat face.*

Figure 3.2: *The difference between the lower flanges.*

3.1.2 Bolts

To ease the meshing, the geometries of the nuts and bolts were simplified, see fig. 3.3. The chamfers on the ends of the bolts were removed and the nuts were transformed to cylinders with the same diameter as the contact surface of the nut. No consideration of the threads in the nut was made, the nut and bolts were modelled as one part. Taking the threads into accounts, the shaft diameter of the bolts were also reduced to a root diameter, defined in ISO 13628-7, Appendix G, Equation G.8 [7]. The threads were not modelled specifically in this project, although the thread interaction was modelled, as described in section 3.2.3.

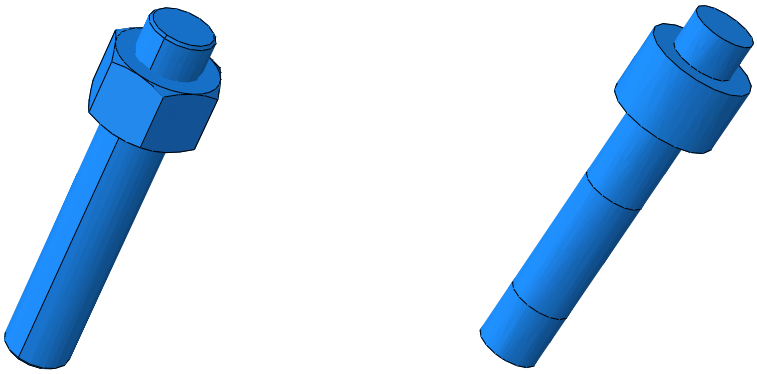

(a) *Original bolt and nut.* (b) *Modified bolt and nut.*

Figure 3.3: *The assembly bolts.*

The bolts were defined as consisting of material ASTM A320 Grade L7M with cold rolled threads with no following heat treatment, see table 3.2 for properties. Compared with cut threads, rolled threads exhibit better fatigue properties.

3.1.3 TX Seal

To provide a tight seal and further improve the performance of the connection a titanium grade 2 TX seal is used between the flanges. This allows hub face separation while preventing leakage and maintaining connection integrity. The use of titanium makes the seal corrosion resistant, reduces the risk of galling and reduces the risk of damage to seat surfaces as compared with a steel seal. The properties of the material can be seen in table 3.2. The geometry of the seal is spherical as seen in fig. 3.4. The advantage of a spherical seal as opposed to a flat

seal is the pressure-energizing property of the spherical seal, meaning when the internal pressure increases, the contact pressure on the seal increases, thus providing better sealing properties. To ease the meshing, small irregularities that would not affect the results, such as small radius's and chamfers were removed.

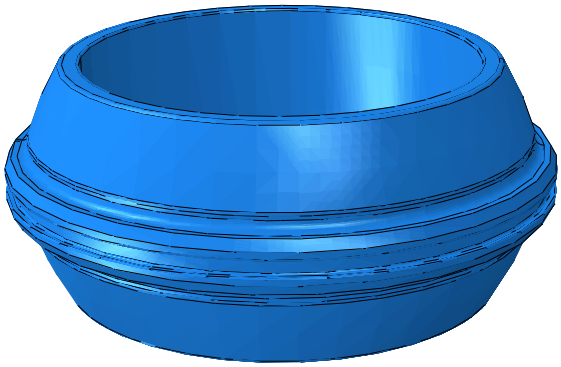

Figure 3.4: *The spherical TX seal.*

3.1.4 Symmetry models

Due to symmetry in both loading and geometry, the assembly was divided in the symmetry plane to decrease the computational cost. The resulting half flanges are seen in fig. 3.5. By doing the partition the loads in tension and bending had to be multiplied by 2 to obtain the load for the complete flange. To model the proper behaviour of the complete flange when using the divided model, proper boundary conditions had to be applied, presented in section 3.2.4.

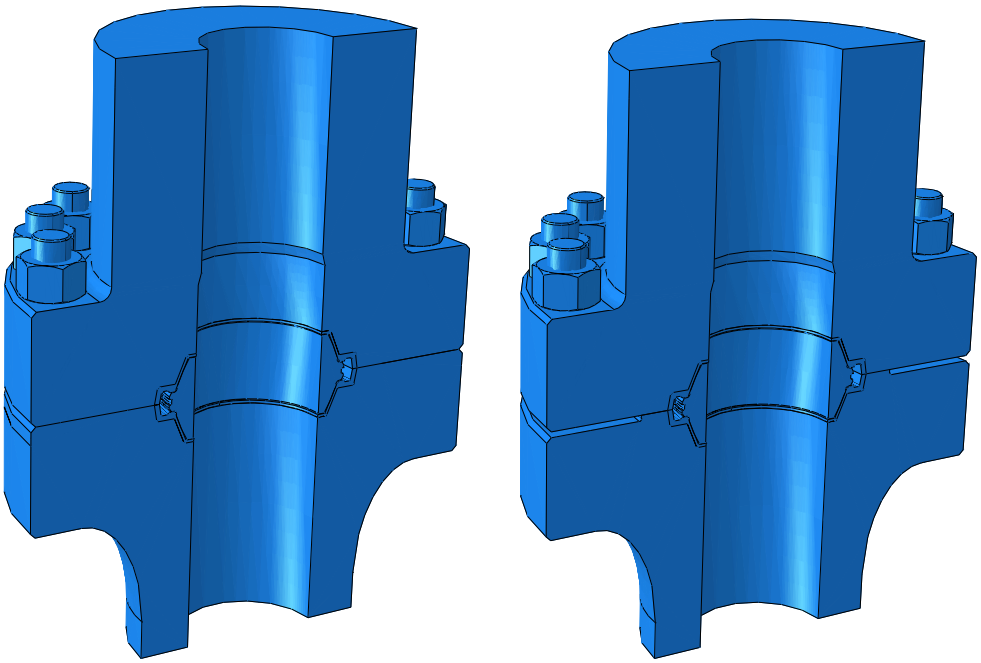

(a) *Flat face flange.* (b) *Raised face flange.*

Figure 3.5: *The symmetry models.*

3.2 Finite element analysis

The analyses were done in Abaqus/Standard, version 6.13-3 and version 6.14-3. To increase computational efficiency it is recommended to enable the use of multiple CPU's for the jobs. To further decrease computational time and since all analyses involve pretensioning of the bolts, it is recommended to create a restart file after the pretension step, the different analyses can then be restarted from this step. For very fine meshes, as in the fatigue analysis, it is necessary to use a submodelling technique, described in section 3.2.6.

3.2.1 The finite element discretization

The geometries were meshed purely using Abaqus C3D8R element. It is a linear hexagonal element using a reduced integration formulation and hourglass control. The reason for using this type of element is explained in section 2.3.1. The mesh sizes varied between the different analyses with a local refinement in the area of interest. The element sizes used during the different analyses can be seen in table 3.1. The number of elements varied from approximately 300 000 for the capacity evaluations to approximately 800 000 for the fatigue analysis.

Table 3.1: The different meshes used during the analyses.

Analysis	Global element size	Refinement region	Local element size
Structural	Flanges: 10 mm, Bolts: 3 mm, Seal: 7 mm	-	-
Leakage	Flanges: 15 mm, Bolts: 7 mm, Seal: 3 mm	-	-
HFS & PLOP	Flanges: 15 mm, Bolts: 7 mm, Seal: 5 mm	Lower hub face	2-3 mm
Fatigue	Flanges: 5-7 mm, Bolts: 1 mm, Seal: 7 mm	Flange radius's	1 mm

For the fatigue analysis, local mesh refinements had to be done in areas with stress concentrations such as the upper and lower radius, as seen in fig. 3.6. In order to provide a smooth transition from the global to the local mesh, adjacent edges were meshed with a biased local seeding.

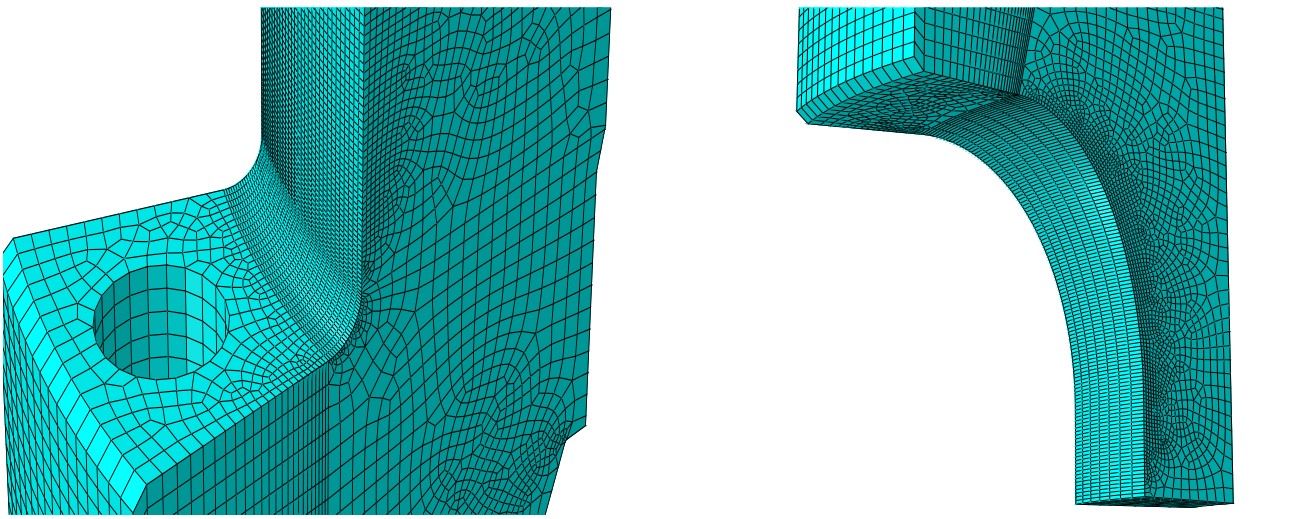

(a) *Refinement on the upper flange.* (b) *Refinement on the lower flange.*

Figure 3.6: *The local refinements on the flange.*

3.2.2 Material model

The materials are modelled using a multilinear elastoplastic model with kinematic hardening up to a point of 0.2% plastic strain after which the material is perfectly plastic. The flange assembly consists of three different materials. The properties are described in table 3.2.

Table 3.2: Material properties.

Material	Elastic modulus	Yield strength	Poisson's ratio	Used for
80 KSI Steel	204 GPa	471 MPa	0.3	Flanges
Titanium Grade 2	102 GPa	249 MPa	0.3	TX Seal
ASTM A320 Grade L7M	198 GPa	502 MPa	0.3	Nuts,Bolts

The stress-strain curves for the materials are presented in fig. 3.7. The dashed lines represents the complete material curves and the filled lines represents the material curves used with a cut off at 0.2% plastic strain. The material data for the 80 KSI steel was only defined up to the 0.2% point, explaining the absence of the red dashed line.

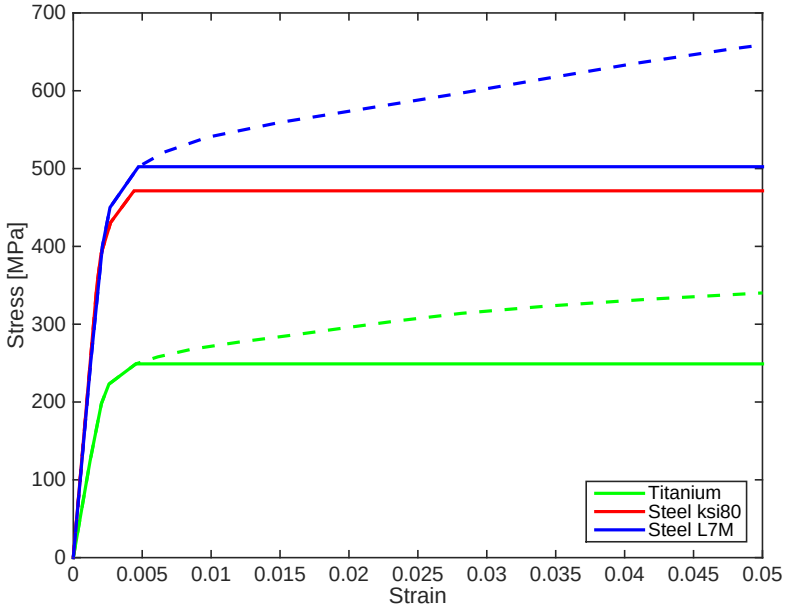

Figure 3.7: *Stress-Strain curves for the material models.*

3.2.3 Contact and coupling properties

To properly model the interactions between the different assembly parts, correct parameters have to be used. Using the incorrect options can result in unwanted penetration of surfaces and artificial contact stresses and other non-physical behaviour. The options used in the present work are presented in the following sections and a further and more detailed description of the options can be found in the Abaqus documentation [16]. When the option of choosing slave and master surface exists, the associated table displays the choice made.

Interaction properties

All of the contacts are defined with both tangential and normal properties. The normal contact is discretized using a surface-to-surface algorithm with a "Hard-contact" option enabled. This option minimizes the surface penetration and ensures no contact pressure when separation between surfaces exists. By default when using the "Hard-contact", the contact algorithm is set to the "Penalty method", described in section 2.5.2.

The tangential behaviour is defined as frictional using a "Penalty" algorithm similar to the one used for normal contact behaviour. This allows a certain amount of transmitted shear stress $\tau \leq \tau_{crit} = \mu\ \sigma_N$ between two surfaces with a contact pressure σ_N and friction coefficient μ, provided they are in contact. The friction coefficient used during the analysis has a value of 0.01. Since the real friction coefficient is uncertain, a low value will not affect the results significantly but rather only stabilize the solver procedure.

Reference points to flange coupling

The boundary conditions and loads are applied on reference points located in the center of the top and bottom surfaces of the flange. The coupling is done using the "kinematic coupling" function in the software. All the degrees of freedom except the radial displacement on the surfaces are coupled to their respective reference point, having the effect that the top and bottom surfaces are free to move in the radial direction independently of the reference points.

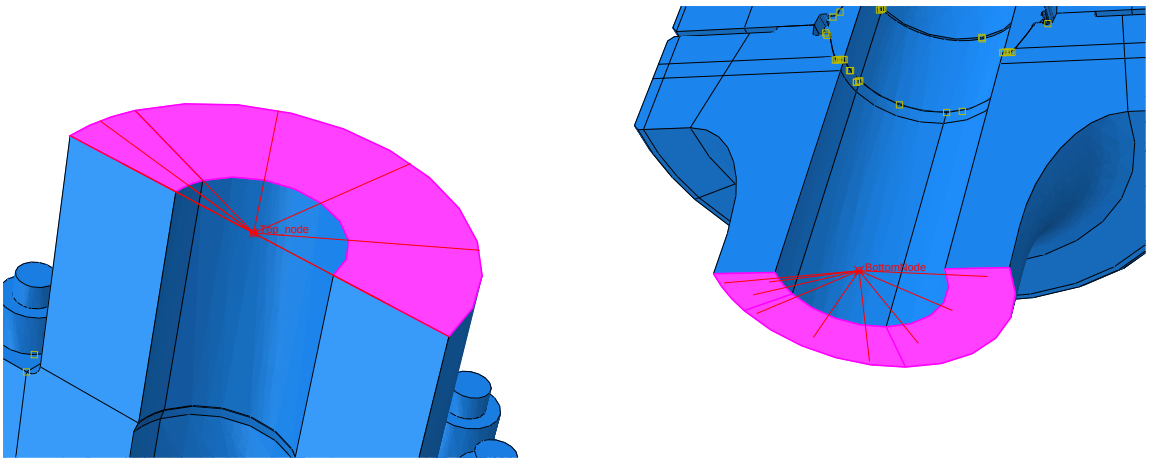

(a) *Top reference point.* (b) *Bottom reference point.*

Figure 3.8: *Kinematic couplings.*

Bolt to upper flange contact

The contact between the bolts and the upper flange is important in order to obtain the correct pretension. Contact is defined between the bottom surface of the nut and the flange surface where the bolts interact, see fig. 3.9. The bolt is set to act as the slave since it will have a denser mesh than the flange.

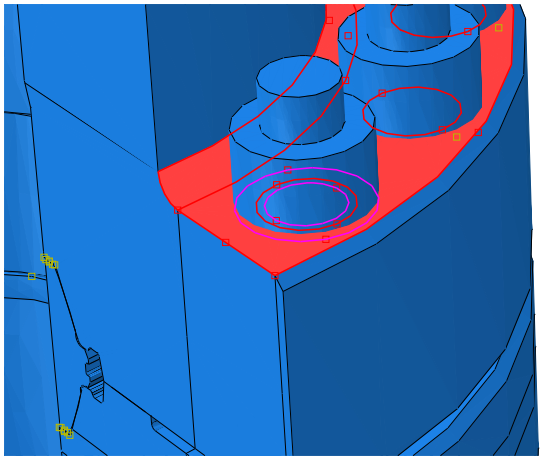

Figure 3.9: *Contact between bolt and upper flange.*

Master	**Slave**
Upper flange	Bolt

Flange to flange contact

The flange to flange interaction definition is seen in fig. 3.10 and fig. 3.11 for the raised face and flat face respectively. The lower flange parts is defined as the slave surface, since a finer mesh on the lower flange will enable a more accurate evaluation of the contact pressure.

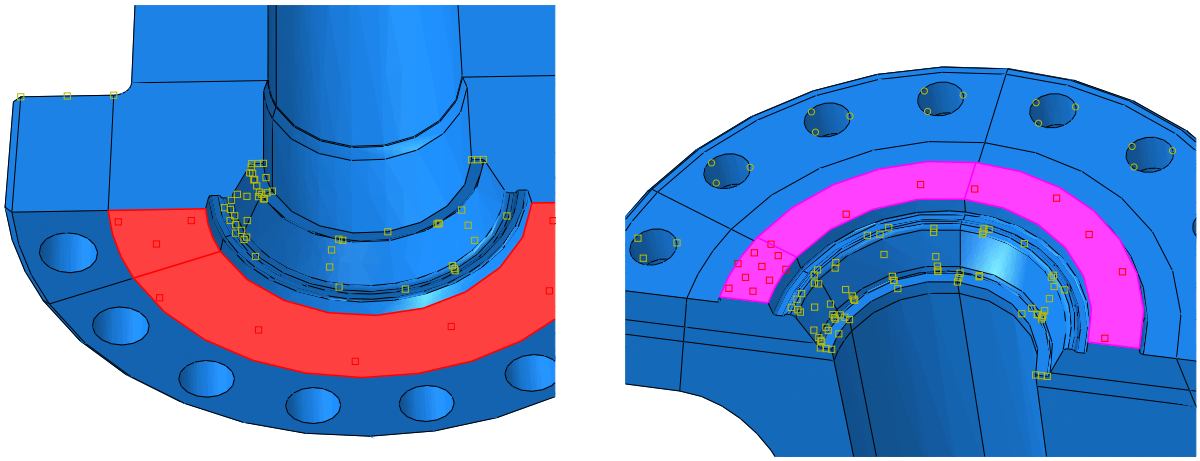

(a) *Master surface on the upper flange.* (b) *Master surface on the lower flange.*

Figure 3.10: *Contact surfaces for the raised face flange.*

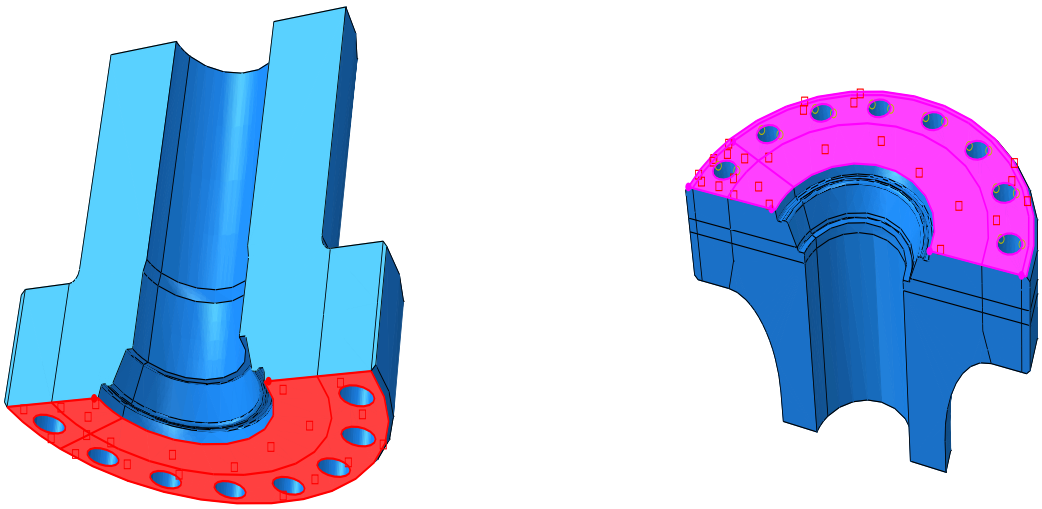

(a) *Master surface on the upper flange.* (b) *Slave surface on the lower flange.*

Figure 3.11: *Contact surfaces for the flat face flange.*

Seal to flange contact

The contact between the seal and the flange are created by dividing the seal into a top and bottom region that are in contact with their respective flange surfaces. The lower master and slave definition can be seen in fig. 3.12.

Master	**Slave**
Flange	Seal

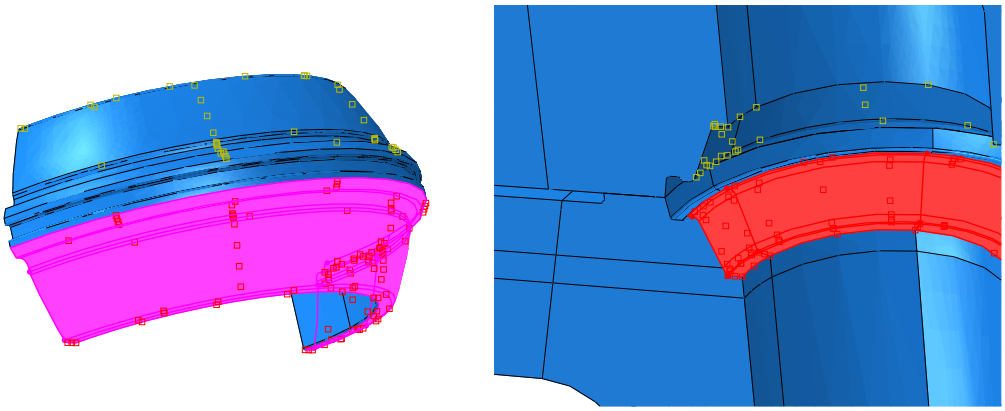

(a) *Lower slave surface on seal.* (b) *Lower master surface on flange.*

Figure 3.12: *The lower area of interaction between seal and flange.*

Surface smoothing is enabled to more accurately model the spherical geometry using the discretized element facets. This will reduce the noise that is created when modelling a spherical surface with flat elements and produce smoother contact fields.

To simulate the assembly of the flanges two methods are available; one is to start with the flanges and seal completely separated and then press the hub faces together in the first load step. This method is not recommended due to convergence issues and an increase of computational time. The other method, used in the present project was to use the "interference fit, shrink" option in the contact editor for the seal to flange contact. This enables a initial face to face contact between the faces of the flanges. The overclosure between the flanges and seal is then removed by moving the nodes in the contact area until the parts are barely in contact. This is done automatically in Abaqus, the software pushes the surfaces apart until there is no penetration. Once the overclosure is resolved, the analysis goes to the nest step. This result is identical to the former method with an significant improvement of the computational time.

Bolt to lower flange coupling

The bolts are connected to the lower flange using the same kind of "tie-coupling" described above. This method has the downside of neglecting the contact between the bolt and bolt hole and thus not taking the stress concentrations in the threads into consideration.

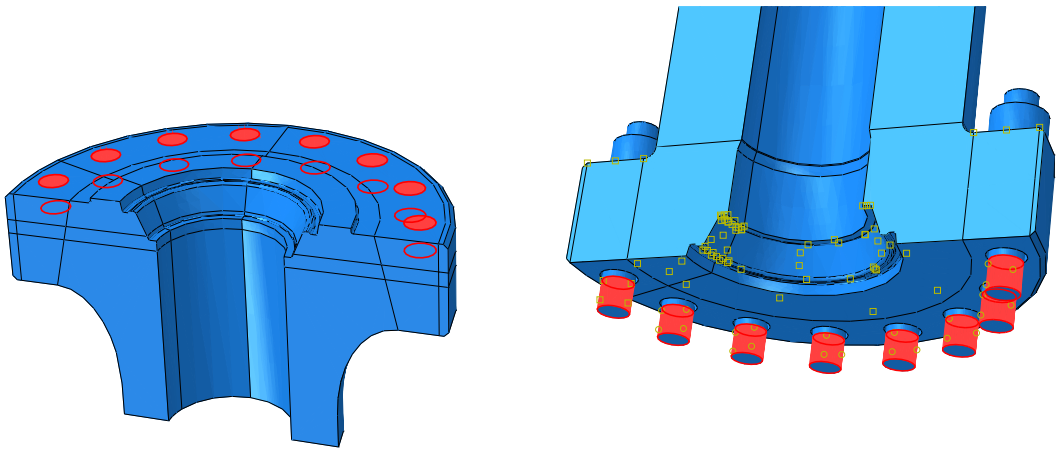

(a) *Tie surface on flange.* (b) *Tie surface on bolts.*

Figure 3.13: *The tie surfaces on the flange and bolts marked in red.*

An alternative to the "tie-coupling" is to use the "threaded interaction" option under the contact pair option. This uses the bolt parameters flank angle, pitch and mean diameter to compute a contact between the bolt and hole. The advantage of using this method is that the singularity in the radius vanishes and the force is distributed along the bolt surface. This is illustrated in fig. 3.14 where it can be seen how the effective von Mises stress field is distributed along the threads of the bolt when using the threaded interaction.

The threaded interaction was used for the fatigue analyses, no difference could be seen compared to the tied option for the other analyses.

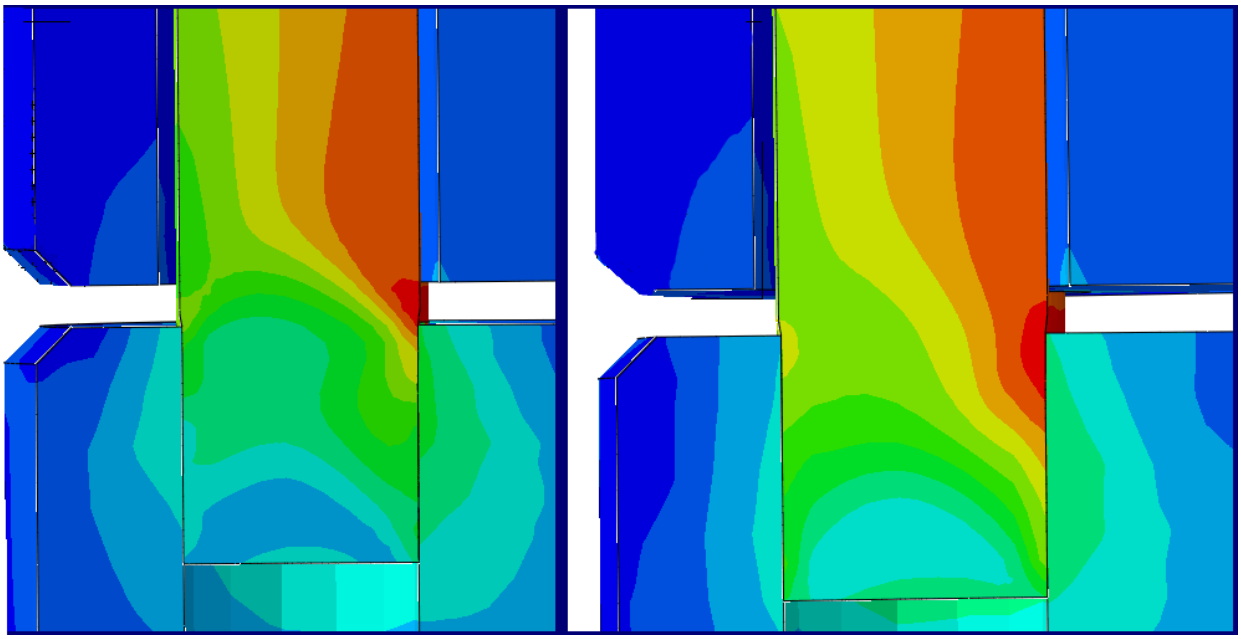

Figure 3.14: *Von Mises stress distribution in the bolt with Tied (left) versus threaded coupling.*

Master	**Slave**
Lower flange	Bolt

3.2.4 Boundary conditions

To model the axisymmetric assumption of the model, proper boundary conditions had to be applied. The bottom reference point was completely fixed using the "Encastre" boundary condition that locks all translational as well as rotational degrees of freedom. The result of this was that the bottom surface of the flange was locked in all directions except the radial.

The axisymmetric condition was obtained by preventing out of plane displacement on the symmetry surface. This is obtained by using the "XSYMM" boundary condition, since in the present case, the normal to the symmetry surface is parallel to the X-axis. The "XSYMM" boundary condition is applied on the symmetry surface as well as on the top reference point, as seen in fig. 3.15.

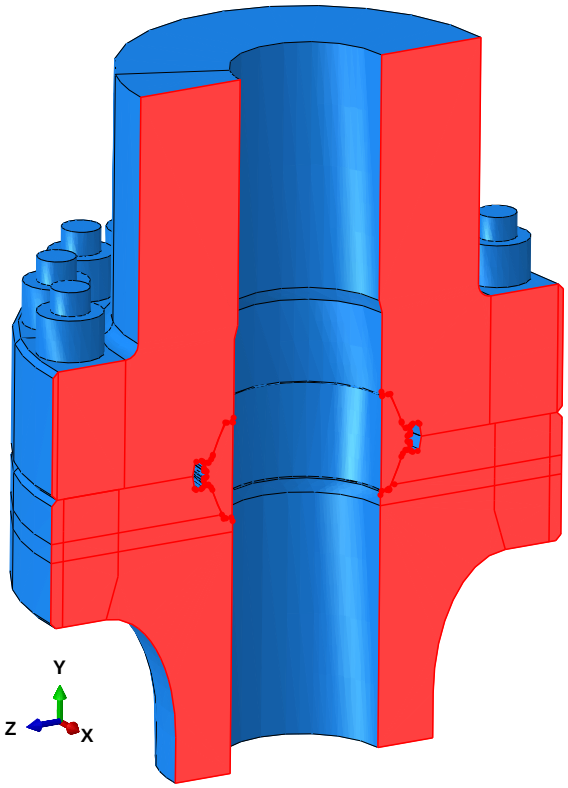

Figure 3.15: *The entities where the XSYMM condition is applied are marked in red.*

3.2.5 Loads

To simulate environmental and operational impact, the flanges are subjected to several loads, consisting of axial tension, bending and internal pressure. The top reference point is used when applying the loads. Due to the symmetric assumption the resulting tension and bending loads were multiplied by 2 to obtain the maximal loads for a complete flange. In addition to the external loads, the bolts were stressed due to an applied bolt pretension, needed to press the hub faces together and secure a tight seal.

When evaluating the structural capacity it is of importance to assure that the connector and not the pipe is the weakest part. In cases when the pipe fails prior to the connector, it is recommended to increase the wall thickness of the pipe section.

Tension

The tensional load is applied in the axial direction of the flange. The load is applied as a concentrated force acting on the top reference node.

Assuming the bolts are the weak points of the structure, an analytical capacity in tension can be calculated as:

$$T_{max} = n \cdot A_b \cdot \sigma_{y,b} \tag{3.1}$$

where

T_{max} is the capacity in tension.
n is the number of bolts.
A_b is the bolt root area.
$\sigma_{y,b}$ is the yield strength of the bolts.

Using Equation (3.1), the analytical capacity in tension is approximately:

$$T_{max} = 16 \cdot 0.02175^2 \cdot \pi \cdot 502 \cdot 10^6 = 11.94 \text{ MN}$$

Bending

To simulate pure bending of the flange a bending moment is applied to the top reference node. The axis of moment is normal to the symmetry surface of the flange.

Using hand calculations according to [7], an analytical capacity in bending can be computed as:

$$M_{max} = T_{max} \frac{BC}{4} \tag{3.2}$$

where

M_{max} is the capacity in bending.
BC is bolt circle diameter.

The analytical bending capacity, using Equation (3.2), is approximately:

$$M_{max} = 11.94 \cdot 10^6 \ \frac{0.5525}{4} = 1649 \text{ kNm}$$

Internal pressure

An internal overpressure, p, was applied on the inner surface of the gasket and flange, see fig. 3.16. The pressure will result in radial forces on surfaces that have normals in the radial direction. Closer to the hub face, due to the geometry of the surfaces, the pressure will also result in axial prying forces attempting to separate the hub faces.

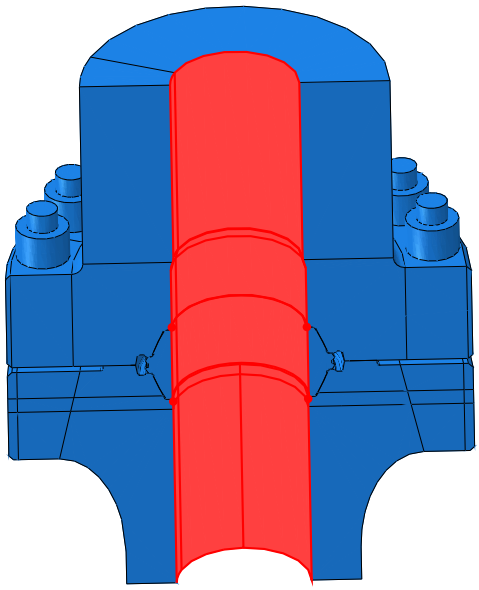

Figure 3.16: *Area subjected to the internal pressure.*

A conservative assumption was used where complete pressure penetration of the joint between the flange and seal was made. See fig. 3.17 for the close up of the pressure penetrated area.

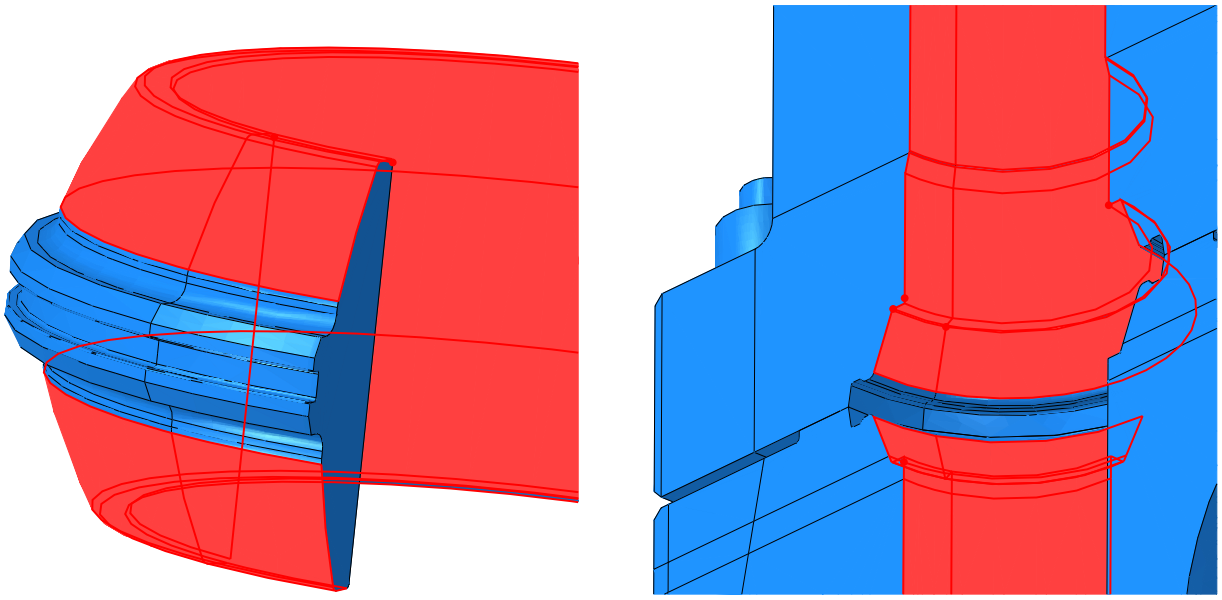

(a) *Zoom in on the pressure area on the seal.* (b) *Zoom in on the pressure area on the flange.*

Figure 3.17: *The areas subjected to the internal pressure on the seal and flange.*

In addition, the internal pressure will create an "end-cap" force, a tensile force acting in the axial direction of the pipe. The end-cap force, F_{endcap} is calculated using the inner radius of the top surface r and the internal pressure p as seen in eq. (3.3).

$$F_{endcap} = p \cdot r^2 \cdot \pi \tag{3.3}$$

Pretension of bolts

Pretension is the effect of applying an initial load on the bolt to fasten the cover and base, thereby, preventing external loads from opening the bolted joint and resisting relative motion between the fastened parts.

The first load step of the analyses consisted of the pretension step. In order to create and maintain a contact pressure the bolts were pretensioned according to industrial standards [7], where an effective bolt stress diameter was used to regard the threaded area. The bolt force was then calculated as the force that would result in a uniform stress equal to 67% of the yield stress.

The bolt pretension was applied in the model using the existing "Bolt pretension" load function where the bolt was partitioned in the axial center and the load was applied on the new surfaces, as described in [21]. The bolt force was then obtained by moving the surfaces a distance d into each other, resulting in a tensional stress in the bolts. The distance d was then held fixed during the rest of analyses.

3.2.6 Submodelling

To be able to analyse models with very fine meshes in critical areas such as, in the present case, the bolts and radius of the flange, it is necessary to use a submodelling technique [16]. When using this approach, the model is split into a global model and a submodel, where the submodel is a partitioned part of the global model including the particular area of interest.

The global model is first solved with a relatively course mesh after which the displacements on the interface between the global and submodel are projected by interpolation to the surface of the submodel. The submodel can then be solved with a refined mesh.

When using the submodel technique it is recommended to partition the global model in the locations of

the submodel. This places nodes on the global model corresponding to the same nodes on the sub model, minimizing the need for interpolation and thus improving the results. It is also recommended to make the partitioning a distance away from the the area of interest, to minimize the influence of the submodelling.

In the present project, the submodelling technique was used for the fatigue assessment since using an element size of 1 mm for bolts and flange's radius would have been too computationally expensive for the complete model.

The submodel consisted of $\frac{1}{8}$ or 22.5^o of the global model, including the most critical areas of the flange in terms of stress variation when subjected to a cyclic bending moment. The submodel and partitioning of the global model can be seen in fig. 3.18.

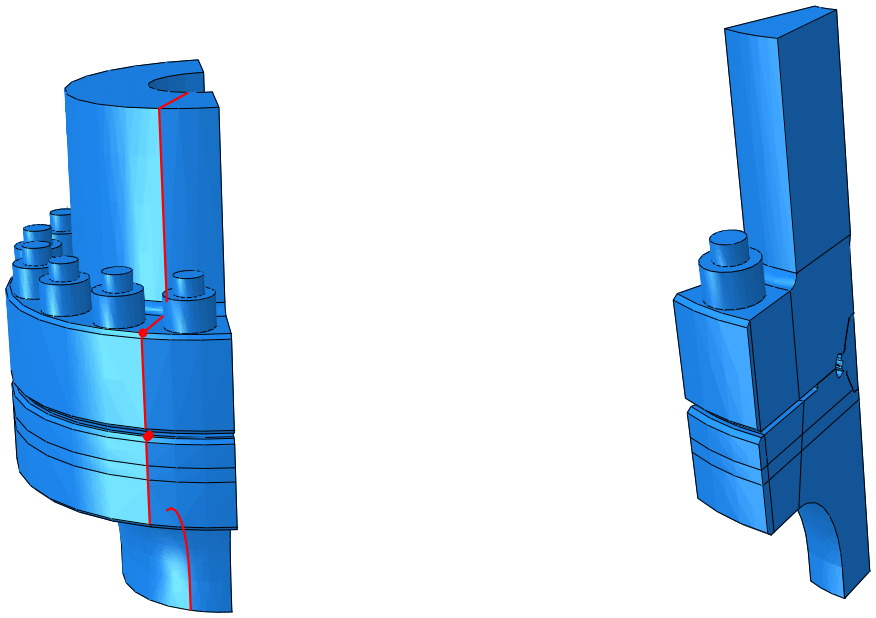

(a) *The global model with the partitioning for the sub model.* (b) *The sub model.*

Figure 3.18: *Models used for the sub model technique.*

3.2.7 Mesh Convergence study

It is well known that the element size of the discretized geometry will affect the results of the analysis. A too coarse mesh will result in an overly stiff model while a too fine mesh will be computationally expensive. It is therefore necessary to perform a mesh converge study. The results from the study, which are the appropriate element size as well as the number of elements and element type, will be used for the proceeding analyses.

According to supervisors, a fine element mesh is more crucial for the fatigue analysis as compared with the structural and functional capacities. This is verified in table 3.4 where the maximal structural capacity in tension is computed for different meshes. The element sizes for the meshes are displayed in table 3.3. The seal was left out to decrease the computational time.

Table 3.3: Element sizes for the different meshes.

	Flanges	Bolts
Mesh 1	17 mm	5 mm
Mesh 2	15 mm	4 mm
Mesh 3	10 mm	3 mm

Table 3.4: The resulting tension capacities.

	Raised face	Flat face	Difference [%]
Mesh 1	11.78 MN	11.78 MN	-
Mesh 2	11.80 MN	11.80 MN	0.17
Mesh 3	11.84 MN	11.94 MN	0.34

From the tables it can be seen that there is only a small difference in capacities for the different meshes, motivating no further refinement of the mesh for the structural and functional capacities.

To examine the mesh converge for the bolts when using threaded or tied options, a simplified model was created consisting of two cylinders representing the bolts and a solid block representing the flange, see fig. 3.20. One bolt was connected using a tie option and the other using a threaded interaction option. A concentrated load was applied to both bolts and the von Mises stresses along the axial direction was extracted. fig. 3.19 illustrates the difference in stress when using the tie or threaded interaction for the bolts. The bolts were modelled with different element sizes, varying from 3 mm to 1.5 mm in steps of 0.5 mm. The left edge of the figure represents the top of the bolt and the right the bottom of the bolt.

As can be seen in fig. 3.19, the stresses converge rather fast in the shank of the bolt and no significant difference can be seen between the finest and coarsest mesh or between the tied and threaded option. The major difference can be seen at the distance 30 mm from the top, where the bolt and flange intersect; when using "tie constraint", a singularity arises due to the sharp edge. Using the threaded interaction this singularity is replaced with a converged increase in stress.

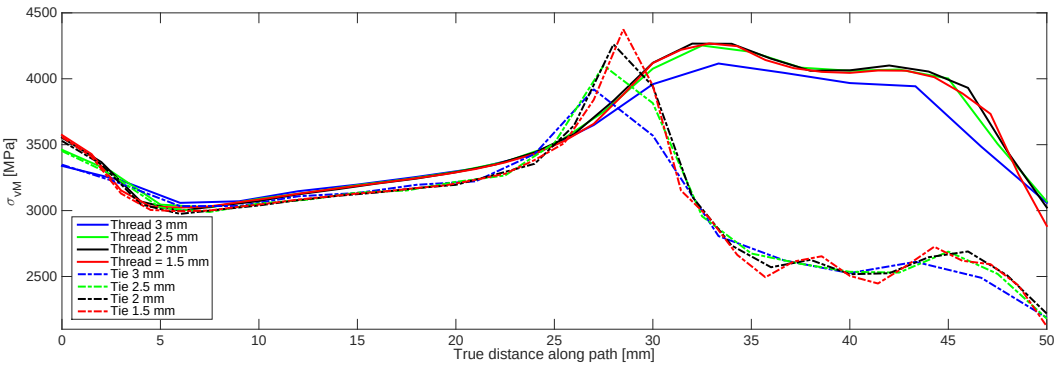

Figure 3.19: *The von Mises stress along the bolt when using tie vs threaded interaction.*

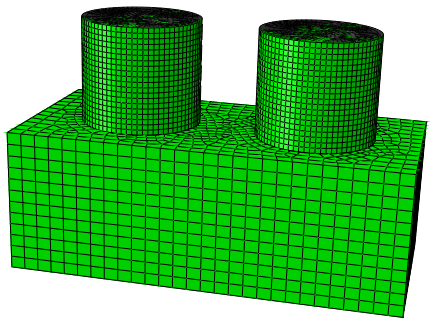

Figure 3.20: *The simplified bolt model.*

A mesh convergence study was also done for the flange's radius. The results can be seen in Appendix A.

3.3 Capacity evaluation criterion

In order to evaluate the capacities of the flange connections, criteria based on the structural as well as functional capacities have to be established. The criteria used are based on industrial standards, [7][8]. The capacities are finally presented in a tabular form as well as graphically, separately for single loads. For a combination of load the capacities are presented as follows:

$$\left(\frac{T}{T_c} + \frac{M}{M_c} + \frac{p}{p_c}\right) \times \frac{1}{F_d} \leq 1 \tag{3.4}$$

Where:

T is the axial separation load tending to separate the connector, [N]
T_c is the axial load capacity (single load) for the applicable failure mode, [N]
M is the absolute value of the externally applied bending moment, [Nmm]
M_c is the bending moment capacity (single load) for the applicable failure mode, [Nmm]
F_d is the design factor,
T_e is the effective tension (externally applied tension) [N]
p is the internal pressure [MPa]
p_c is the internal pressure (single load) capacity, including end-cap effect. [MPa]

The combined load assumes that the capacities varies linearly, a conservative assumption made according to industrial standards.

3.3.1 Structural capacity criterion

The structural capacities are evaluated using an industrially approved best practice method. Accordingly, the plastic material properties are defined up to a point of 0.2% plastic strain, after which the material is ideally plastic, see fig. 3.7.

To evaluate the capacities of the flanges in terms of maximum tension, bending and pressure, the applied loads will be ramped up to a load resulting in plastic strains in a cross section exceeding the last defined plastic point, i.e. 0.2%, this results in diverging equilibrium iterations. The maximum loads can then be evaluated as the last loads that resulted in a converging solution.

3.3.2 Functional capacity criterion

The functional capacities will be evaluated using a leakage-, a hub face separation- and a loss of pretension criterion for the load cases of axial tension, bending and internal pressure.

Leakage

According to industrial methods [7] [8], the leakage capacity is evaluated using the contact pressure c_p, along a distance c_d, on the seal, according to industrial guidelines. The criterion state that:

$$\begin{aligned} &c_p \geq \max(100, 3 \cdot p)\,\text{MPa, where } p \text{ is the internal pressure} \\ &c_d \geq 2\,\text{mm} \end{aligned} \tag{3.5}$$

Due to difficulties evaluating the minimum pressure distance, c_d, the contact pressure criterion has been transformed previously in best practice reports to a specific contact force criterion for this specific seal. The contact force q is computed by integrating the contact pressure, c_p, along a path, s, on seal's contact surface as:

$$q = \int_s c_p \, dx$$

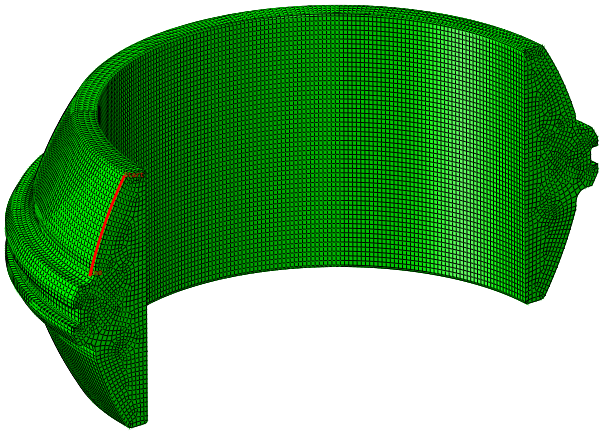

Figure 3.21: *Path along the seal surface.*

In fig. 3.21, the path along the seal surface is shown. The specific contact force has the unit of force per length and it will be calculated from a path on the seal where the risk for leakage is highest. In the cases of tension and pressure, the contact pressure is equal on the seal so it does not matter where the contact force is calculated, but for bending case, the part of the seal that is compressed, will have higher contact pressure. The criterion for the specific contact force is the evaluated as:

$$q \geq \max\ (480.3, 14.42 \cdot p)\ \ {}^{\mathrm{N}}/_{\mathrm{mm}} \tag{3.6}$$

The seal is allowed to plastically deform provided that the contact force is maintained at an acceptable level.

Hub face separation

Hub face separation is defined as the point when complete separation occurs between the two mating hub faces along the radial direction. The separation can be divided into two principally different separation growth direction:

- Separation initiates at the inside and grows outwards.
- Separation initiates at the outside and grows inwards.

The behaviours are illustrated in Figure 3.22.

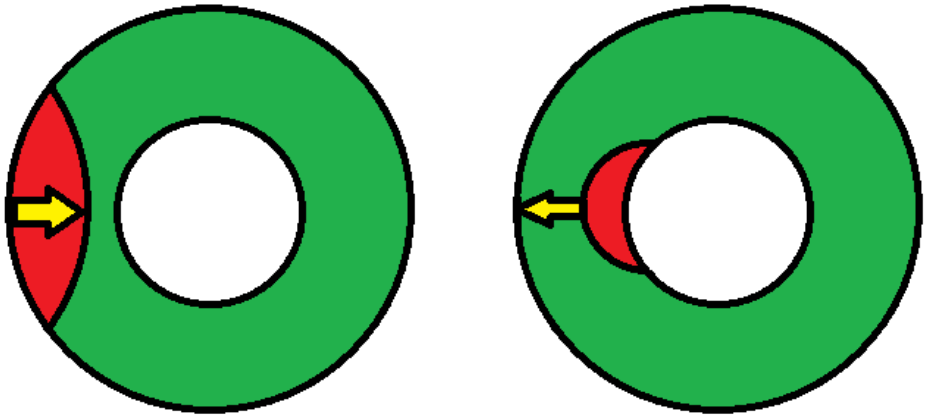

(a) *Inwards propagation.* (b) *Outwards propagation.*

Figure 3.22: *The two modes of hub face separation, the yellow arrow displaying direction of propagation.*

The inside initiation and outwards propagation is the more severe case since it decreases the contact pressure at the seal and increases the risk of leakage, as compared with the inwards propagating case.

To evaluate the face separation, the minimum contact pressure along a tangential path, see fig. 3.23, was evaluated for each increment. When the contact pressure equals zero, the faces have separated completely. The capacity will then be evaluated as the last load before the hub faces are completely separated.

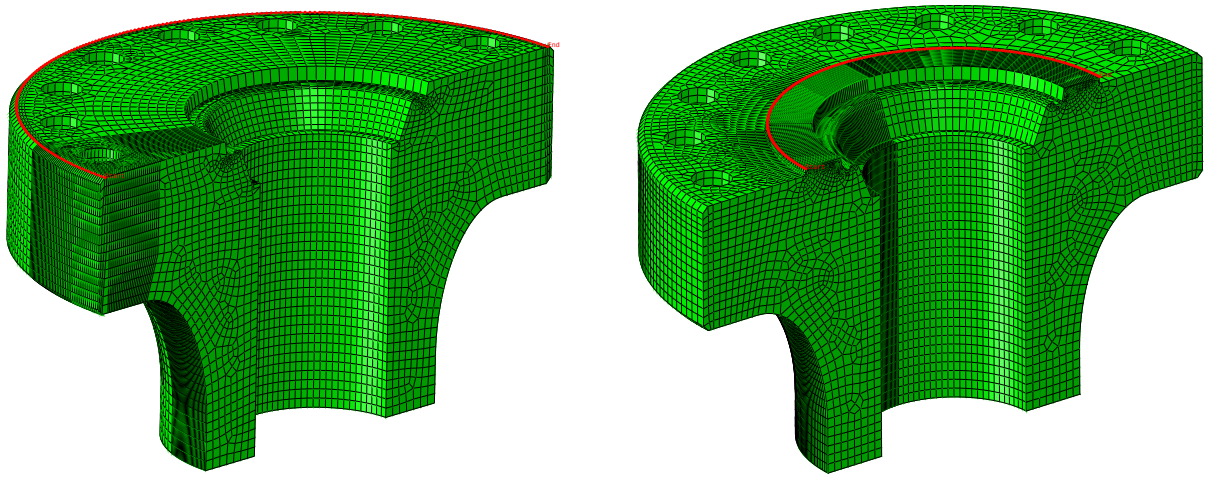

(a) *Node-path in flat face flange.* (b) *Node-path in raised face flange.*

Figure 3.23: *Node-paths for evaluation of HFS-capacity.*

Loss of pretension

Loss of pretension (LoP) or loss of hub face separation capacity occurs due to the bolts yielding and obtaining plastic strain. The plastic strain will decrease the pretension on the assembly and thus separation will occur at a lower load. The capacity is evaluated according to TR 3541 [8]. The procedure consists of applying a load "X" that results in yielding of the bolts. The load "X" should typically be 15-25% above the separation point, but less than 80% of the structural capacity in tension or less than 67% of the structural capacity in bending. The load is then released and re-applied until separation occurs at load "Z", see fig. 3.24. The remaining pretension capacity can then be calculated as:

$$z_i = \frac{Z_i}{Y} \tag{3.7}$$

where Y is the separation capacity and the index "i" signifies different loads X.

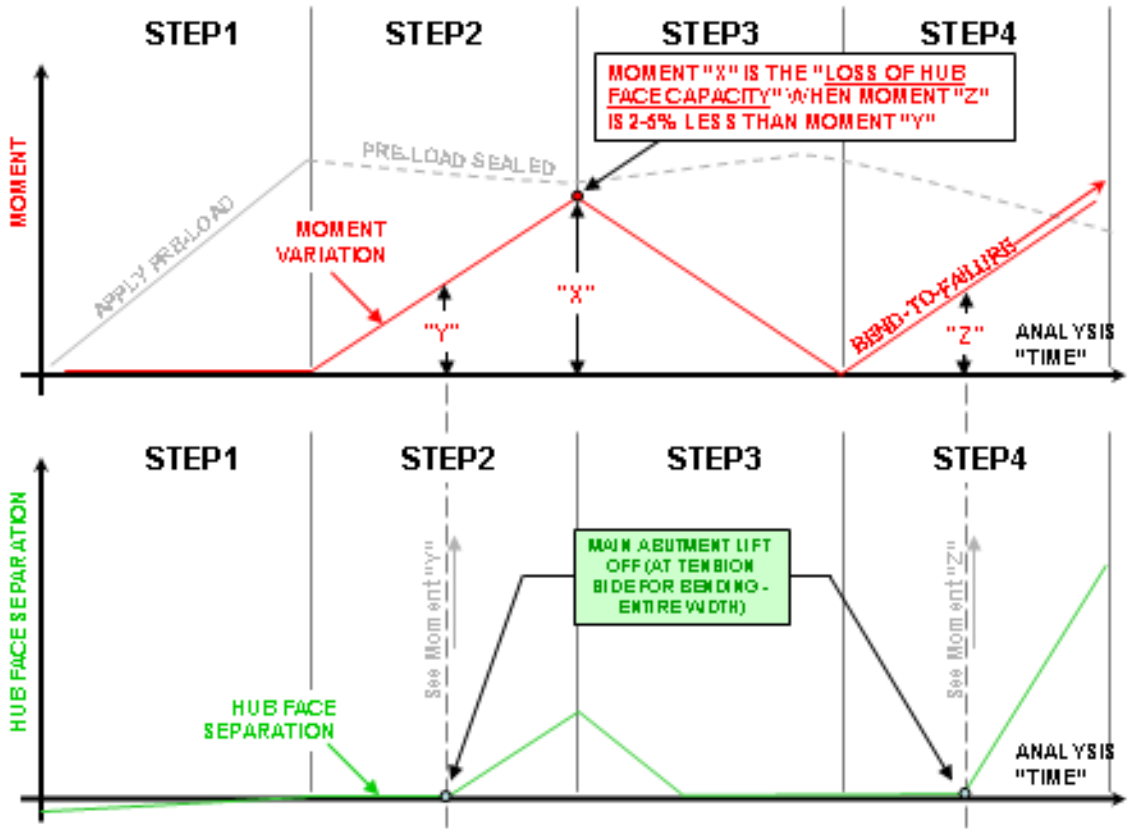

Figure 3.24: *The analysis steps to evaluate LoP [8].*

The results can then be summarized in Table 3.5.

Table 3.5: Summary table of LoP.

Load	Remaining capacity
X_i	z_i
$\vdots$	$\vdots$

3.4 Fatigue analysis

The fatigue analysis will consider a high cycle fatigue (HCF) approach. The reason for this is that the cyclic loads are mainly a result of environmental influences, as stated in Appendix C in [9]. Considering a wave period of 10 seconds and a service life of 5 years the expected life can be calculated as:

$$5 \cdot 365 \cdot 24 \cdot 60 \cdot 60/10 = 15768000 \text{ cycles}$$

Low cycle fatigue (LCF) is roughly described as a life time of 10^4 cycles [19]. Using this, the components life can be calculated as $10 \cdot 10000/60/60/24 = 1$ day, motivating the use of a HCF approach.

Since fatigue was analysed by evaluating the stress range variation, the stress from the pretension step had to be subtracted from each load increment. The resulting stress field could then be used for the fatigue assessment. In accordance with ISO 13628-7 [7], the component life will be expressed as:

$$log\ N = log\ \bar{a} - m \times log \left[S \times \left(\frac{t_n}{t_{ref}} \right)^{k_1} \right] \tag{3.8}$$

Where

N is the number of expected cycles to failure.

$\bar{a}, m, k_1$ are constants for the specific S-N curve

S is the stress range obtained from the FE analysis

The fatigue life was evaluated using a stress transfer function to relate the applied bending moment to stresses in hot spots. A hot spot is a point in the structure where a fatigue crack will most likely grow due to the combined effect of structural stress fluctuation. The fatigue analysis was then performed using the stress range values in hot spots. To relate the multiaxial stress state to a equivalent uniaxial stress four different methods were used; the von Mises stress range, an effective stress range according to Manson-McKnight, see eq. (3.9) [20], the maximum principal stress range and the axial stress range. In the presence of compressional stresses, the stress range was reduced by a factor f_m, as stated in [9]. The factor can be calculated as:

$$f_m = \frac{\sigma_t + 0.6\ \sigma_c}{\sigma_t + \sigma_c} \qquad \text{where} \qquad \begin{cases} \sigma_t \text{ is the maximum tension stress} \\ \sigma_c \text{ is the maximum compression stress} \end{cases}$$

The material fatigue data was obtained as S-N curves from DNV RP-C203 [9]. The hotspots on the flange used curve B1[1], see eq. (3.10). The threads in the bolt used a reduced curve compared with the other parts, F1[2], see eq. (3.11), to take into account the stress concentrations in the threads.

$$\Delta\sigma_{eq} = \frac{1}{\sqrt{2}} \times \sqrt{\left[(\Delta\sigma)_1 - (\Delta\sigma)_2\right]^2 + \left[(\Delta\sigma)_1 - (\Delta\sigma)_3\right]^2 + \left[(\Delta\sigma)_2 - (\Delta\sigma)_3\right]^2} \tag{3.9}$$

$$\begin{aligned} \log(N) &= 15.117 - 4\ \log(S) \qquad \text{For stress range } S > 106.97\,\text{MPa} \\ \log(N) &= 17.146 - 5\ \log(S) \qquad \text{For stress range } S \leq 106.97\,\text{MPa} \end{aligned} \tag{3.10}$$

$$\begin{aligned} \log(N) &= 11.699 - 3\ \log(S) \qquad \text{For stress range } S > 36.84\,\text{MPa} \\ \log(N) &= 14.832 - 5\ \log(S) \qquad \text{For stress range } S \leq 36.84\,\text{MPa} \end{aligned} \tag{3.11}$$

The results from the fatigue analysis are presented as M-N curves, relating an alternating bending moment range to the estimated number of cycles to failure calculated by eq. (3.10) and (3.11). The use of a bending moment as a fatigue load was motivated due to the environmental variational loads consisting mainly of bending.

[1] 160 according to IIW and Eurocode 3 notation

[2] 63 according to IIW and Eurocode 3 notation

4 Results & Discussion

The results from the analyses evaluated according to the previous methods are presented below. A similar behaviour is seen for all capacities; when the flanges were loaded in either tension or pressure no difference in performance could be seen. When loaded in bending the flat face flange performed significantly better.

4.1 Structural capacities

The resulting structural capacities are presented in table 4.1. A further discussion of the separate load cases are provided in the following sections.

For the load cases of tension and bending, the bolts were the limiting components, i.e. the maximum stress was located in the assembly bolts. When loaded with an internal pressure the maximum stress was located in the seal as explained in in section 4.1.3. As can be seen in table 4.1, the raised face and flat face exhibited the same structural capacities except in the case of bending, where the flat face flange could be subjected to a higher bending moment.

Table 4.1: The resulting structural capacities.

Load case	Raised face	Flat face
Tension [kN]	11848	11846
Bending [kNm]	2070	2916
Pressure [MPa]	230	233

4.1.1 Capacity in tension

There was no major difference in the structural tension capacities between the two flanges. The capacities for the raised face and the flat face flange were evaluated to 11.848 MN and 11.846 MN respectively. Compared with the analytical prediction of 11.94 MN, calculated in Section 3.2.5, the results from the FEA differs around 0.8%.

Figure 4.1 presents the equivalent plastic strain for the last converged increment. The black field represents regions where the equivalent plastic strain exceeds 0.2%. As can be seen, the cross section of the bolts have fully yielded, indicating failure of the flange. Further, no significant difference can be seen between the flanges.

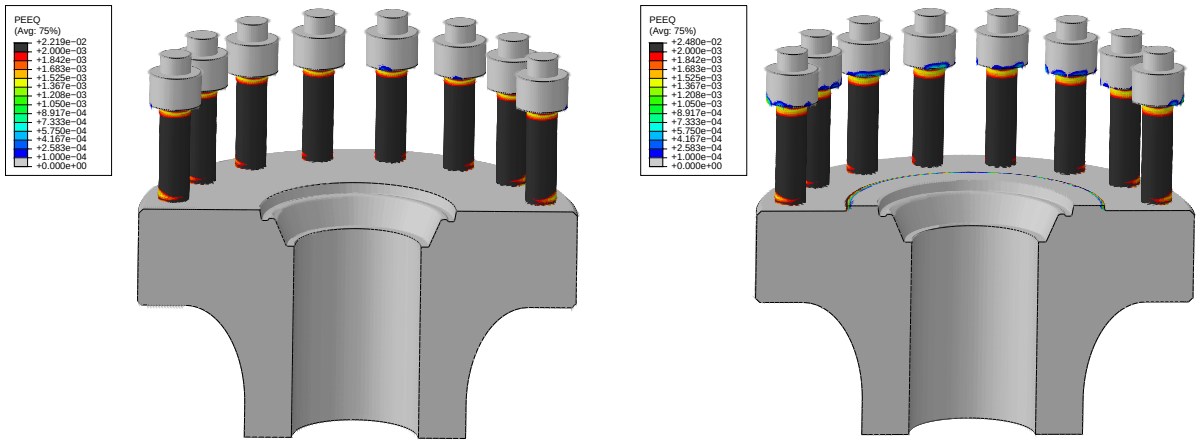

(a) *Flat face.* (b) *Raised face.*

Figure 4.1: *Equivalent plastic strain in the flanges.*

4.1.2 Capacity in bending

The structural bending capacity of the raised face flange was evaluated to 2070 kNm. The flat face flange could be subjected to a higher bending moment compared to the raised face flange, due the the stiffening effect of the larger hub face contact surface. For this reason, the structural failure did not occur in the bolts for the initial geometries as in the case with the raised face flange. Instead, the lower flange was the limiting component, i.e. the plastic strain through thickness exceeded the maximum level in the lower pipe. The maximum bending moment that could be applied was 2420 kNm before the pipe failed. This can be seen in fig. 4.2, where the black field is the region where the equivalent plastic strain is equal to or higher than 0.2%. As seen in the figure, for the raised face flange, the bolts that are loaded have yielded through the cross section. Whereas, in the flat face flange, there is still one bolt left that can carry the applied load.

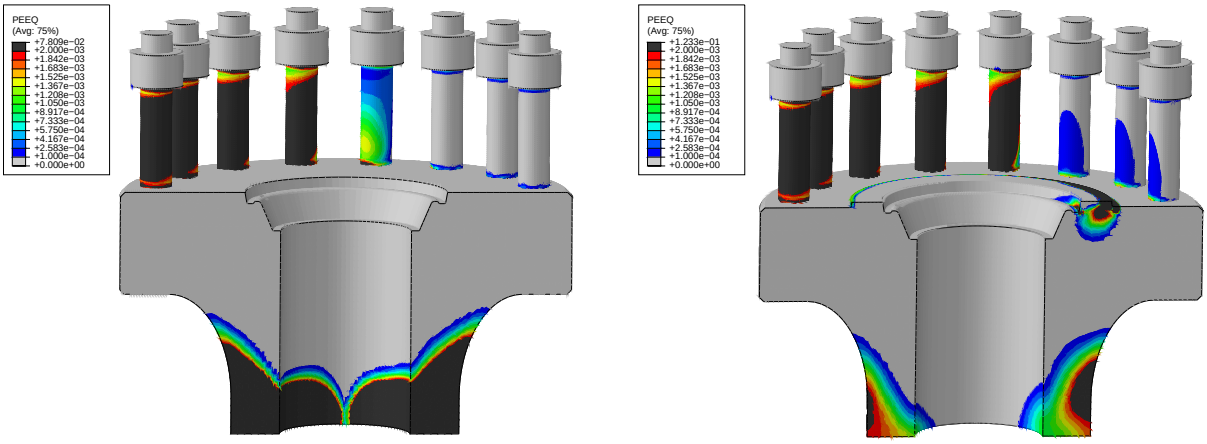

(a) *Flat face.* (b) *Raised face.*

Figure 4.2: *Eqivalent plastic strain in the flanges.*

Since it was required to find the actual connector capacity, i.e. the capacity of the bolt assembly, a stronger pipe section had to be modelled to ensure that the failure would not occur in the pipe. This was done by increasing the wall thickness of the lower pipe by 30 mm, see fig. 4.3.

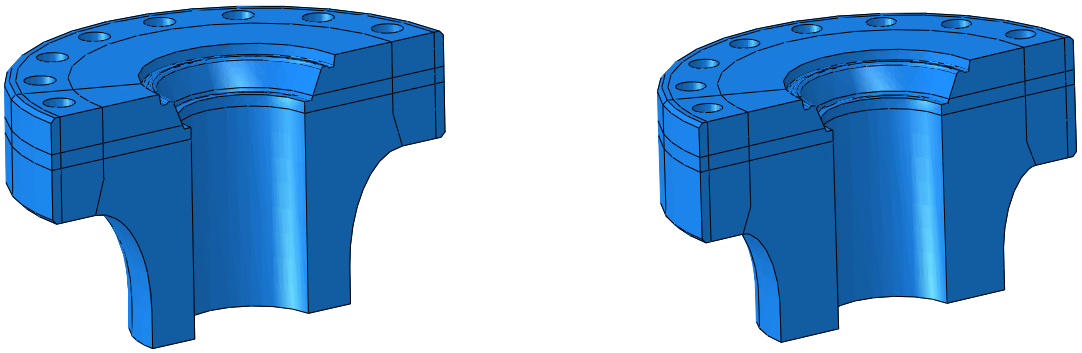

(a) *Orginal model.* (b) *Modified model.*

Figure 4.3: *Lower flange.*

The structural bending capacity was calculated again and the maximum bending moment that the flat face flange could carry out increased to 2916 kNm before the bolt assembly failed, see fig. 4.4. Compared to the analytical solution, the results differed by 22% and 42% for the raised face and the flat face flange respectively. The large difference between the analytical and the FE-results are due to the complex behaviour of the flange in bending. Additionally, the analytical equation only uses the tension capacity and the bolt circle diameter as parameters, not taking the geometries into consideration.

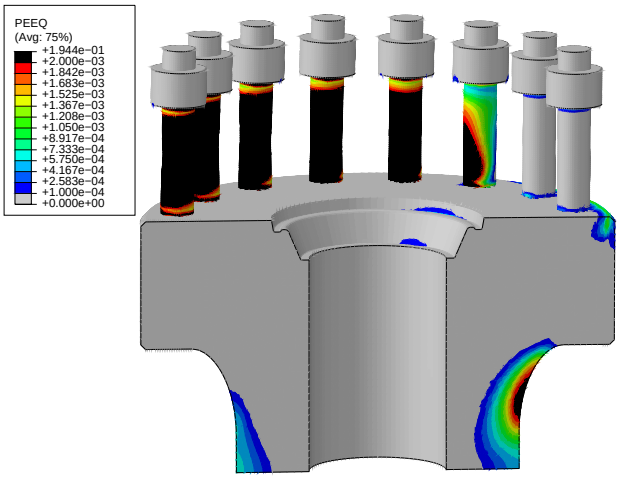

Figure 4.4: *Equivalent plastic strain in the flat face flange.*

4.1.3 Capacity in pressure

The difference in structural capacity between the flanges when subjected to an internal pressure was small. The capacity in pressure resembles the capacity in tension due to the end-cap force acting as a tension load. The initial models reached structural failure before the cross section of the bolts were fully yielded. This was due to the fact that the seal was completely yielded, see fig. 4.5, at 194 MPa, but as mentioned in the previous section, since the actual connector capacity is sought, i.e the capacity of assembly bolts, this results could not be considered as structural failure. In order to get the actual capacity, the analysis was repeated with an extended stress-strain curve for the seal, allowing more hardening. The structural pressure capacities were now calculated to 233 MPa for the flat face flange and 230 MPa for the raised face.

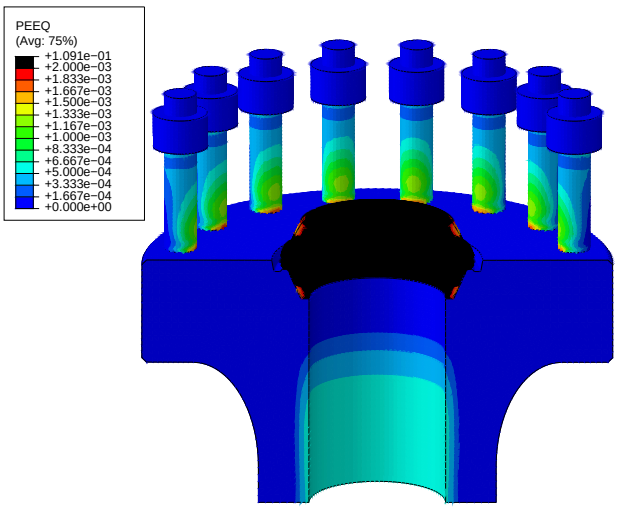

Figure 4.5: *The seal fully yielded.*

4.2 Functional capacities

The functional capacities are evaluated according to section 3.3.2 and the results are presented in the following sections.

4.2.1 Hub Face Separation (HFS)

The hub face separation (HFS) capacity for the flanges are presented in table 4.2. For all of the load cases the separation initiated from inside and propagated outwards.

Table 4.2: The resulting hub face separation capacities.

Load case	Raised face	Flat face
Tension [kN]	9800	10120
Bending [kNm]	1028	1320
Pressure [MPa]	188	211.3

Figures 4.6-4.7 display how the minimum contact pressure along a tangential path, see fig. 3.23, on the mating hub faces varies during loading.

Figure 4.6a shows how the smaller contact surface of the raised face flange results in a relatively higher contact pressure of approximately 520 MPa after preload, as compared with a contact pressure around 100 MPa for the flat face flange. When the load was increased, the contact pressure on the raised face flange decreased almost linearly to the minimum value while for the flat face, the contact pressure had a small increase at the beginning of loading until half of the separation capacity was applied. The contact pressure stayed then almost constant until it approached the maximum separation force, where it fell rapidly to zero.

The difference in behaviour is due to the location of the last contact point on the hub faces. When the hub faces start separating, the flanges will rotate around a pivot point. The pivot point, for a path from inner radius to outer, is the last point that will separate and therefore the point experiencing the largest contact pressure. On the flat face flange the pivot point is located outside the bolt circle as opposed to the raised face flange, where the pivot point is located on the inside of the bolt circle.

The same behaviour can be observed for the case of an applied bending moment as well as an applied internal pressure.

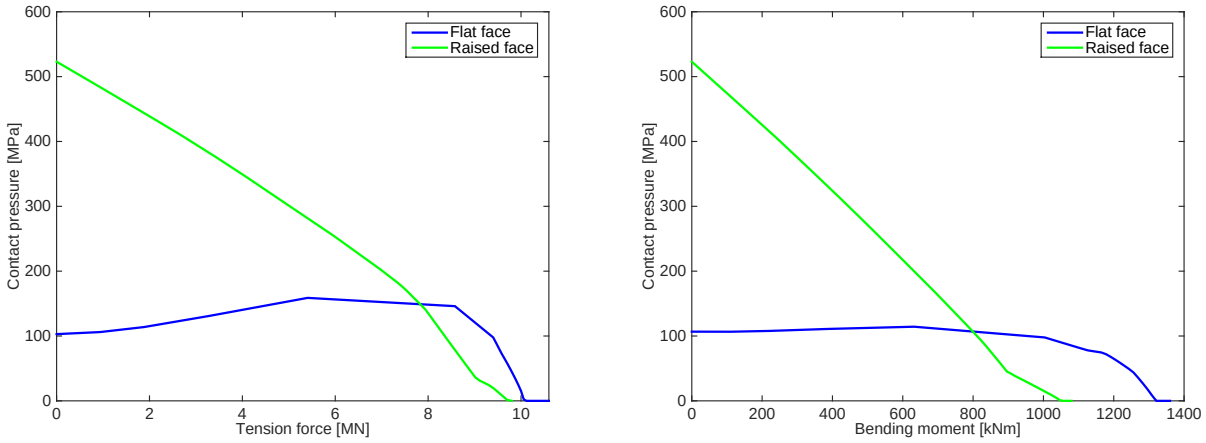

(a) *Applied tension.* (b) *Applied bending.*

Figure 4.6: *Minimum contact pressure on the tangential path.*

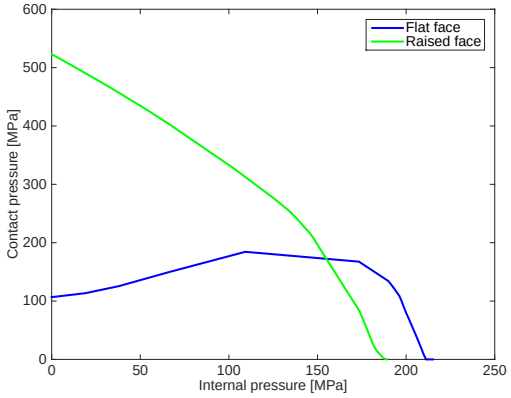

Figure 4.7: *Minimum contact pressure on the tangential path, applied internal pressure.*

4.2.2 Leakage

The specific values for the leakage capacities have been removed due to requests from Aker Solutions. The present leakage section only presents the overall behaviour of the capacity.

Figures 4.8 - 4.9 show how the specific contact force for the flanges varies with increasing load. It is noticed how the specific contact force after preloading is relatively high for both flanges, with a slightly higher value for the raised face flange due to flange rotation.

In fig. 4.8a the specific contact force is plotted versus the tension force. Due to the absence of an internal pressure, the specific contact force is constant. As one can observe, when the load is increased, the contact force stays unchanged for a large part of the loading, although when approaching the maximum load there is a sharp drop in force until the the criteria is no longer satisfied.

In fig. 4.8b, one can see how the specific contact force varies with increasing bending moment. The initial behaviour is similar to the one seen in fig. 4.8a, with the raised face flange managing to maintain the contact force better than the flat face at the beginning of loading. This suggests that for low to moderate loads up to 50% of the maximum leakage load, the leakage capacity is somewhat better for the raised face flange. However, when the load is increased further, the specific contact force for the raised face flange decreases faster compared to the flat face. At a moment of slightly below 75% of the raised face capacity, the two curves cross, after which there is a rapid drop for the raised face flange. The result is resembling the result seen for the structural bending capacities, where the flat face flange could endure a higher bending moment.

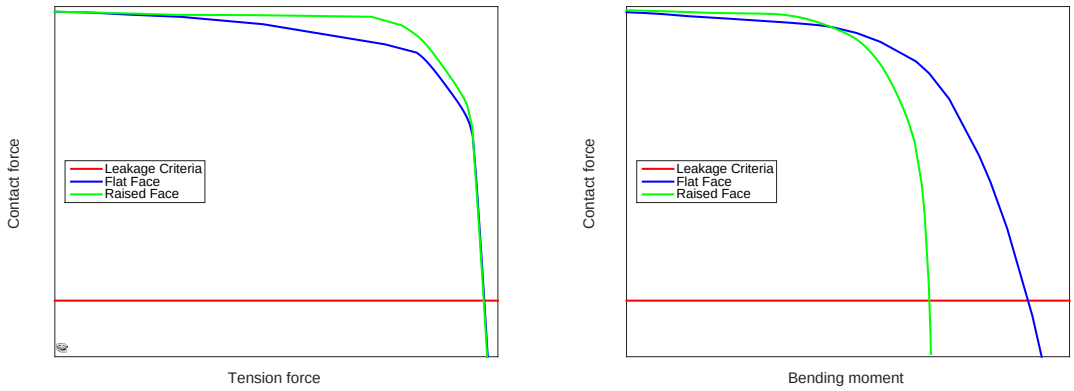

(a) *The leakage capacity in tension.*

(b) *The leakage capacity in bending.*

Figure 4.8: *The specific contact force versus applied load.*

Figure 4.9 displays how the contact force varies when the assemblies are loaded with an internal pressure. The leakage criterion is now also varying with the internal pressure as opposed to the two previous load cases of tension and bending. In initial analyses the flange did not show any signs of leakage, despite the pressure reaching the structural capacity limit. This was due to the large plastic strains in the seal, seen in fig. 4.5. Therefore, the pressure leakage analyses were remade with an extended material curve allowing more hardening of the titanium.

Using the extended material curve, still no leakage occured and the pressure could be increased up to the point of structural failure. Although, as can be observed in fig. 4.9a, just before structural failure, the specific contact force decreases rapidly, but still satisfies the criterion. However, examination of the results from the previous load cases of tension and bending, one can assume that the specific contact force will go towards zero quickly with a small increase of internal pressure, therefore it can be concluded that leakage occurs at the same time as structural failure.

In fig. 4.9a, the specific contact force criterion eq. (3.6), is used and in fig. 4.9b the contact pressure criterion eq. (3.5), is considered. Using the contact force criterion resulted in the same capacities as using the contact pressure criterion for the loads of tension and bending, however for evaluating the leakage capacity for the internal pressure, there was an inconsistency between the contact force and contact pressure criterion. When the contact pressure criteria is considered and using the cut-off material model, the contact pressure will fall below the minimum required contact pressure when the internal pressure reaches a moderate magnitude.

A reason for this could be due to the plastic strains occurring in the seal at a high pressure. From the results it could be seen how the contact area on the seal grew when the load was increased. The larger contact area could result in a decreased contact pressure even though the load on the seal increased. Another reason for the difference could be that the contact pressure criterion should be applied when a fine mesh is used for the seal. The element size used to mesh the seal was 3 mm, but according to supervisors at Aker Solutions, when using the contact pressure criterion the element size for this analysis should be much smaller than the minimum contact length, i.e. smaller than 2 mm.

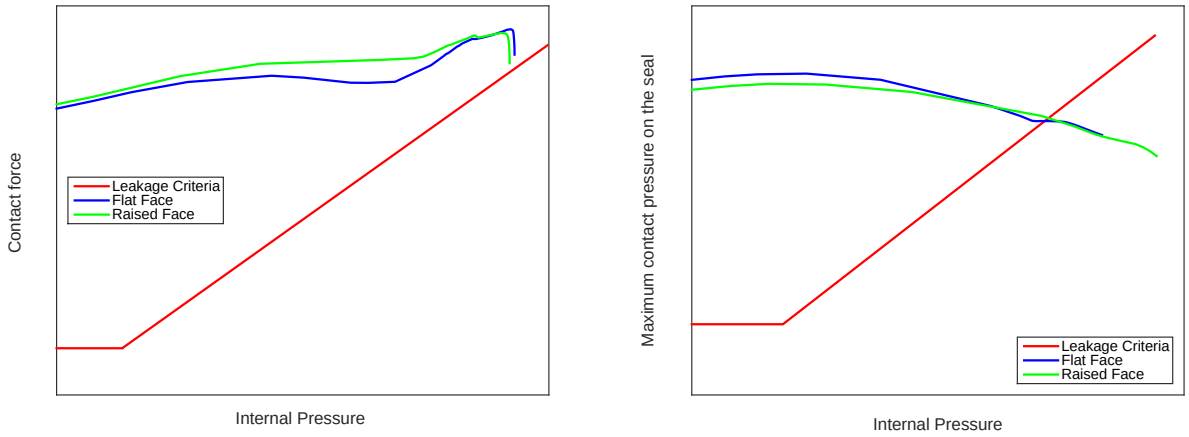

(a) *Specific contact force versus internal pressure.*

(b) *Contact pressure versus internal pressure.*

Figure 4.9: *The different leakage criterion.*

4.2.3 Permanent Loss Of Pretension (PLOP)

As described in Section 3.3.2, the plastic strain in the bolts decreases the preload force, meaning that the separation happens earlier when the flange is reloaded and thus the preload capacity is reduced. The results of the permanent loss of pretension for the flanges are presented in Tables 4.3 - 4.8 and Figures 4.10 - 4.12. For a better comparison between the flanges, the applied loads, AL_i, have been normalized using the following equation:

$$AL_i = \frac{AL_i}{AL_1}, \qquad i = 1, 2, 3, ...$$

As mentioned before, the hub face separation capacities in tension for the raised face and the flat face flanges were evaluated to 9.80 MN and 10.12 MN respectively. In Tables 4.3 and 4.4, the magnitudes of tension that have been applied to the flanges and the corresponding remaining preload capacities are shown.

Table 4.3: The resulting PLOP for tension of raised face flange.

Load [MN]	Remaining capacity
10	98.8%
10.8	87.4%
11.2	76.6%
11.6	63.0%

Table 4.4: The resulting PLOP for tension of flat face flange.

Load [MN]	Remaining capacity
10.2	99.0%
10.4	96.8%
10.8	81.5%
11.2	61.2%
11.6	26.3%

In fig. 4.10, the remaining preload capacity or remaining separation capacity after different magnitudes of loading in tension is plotted. As can be seen, the raised face flange manages to retain the pretension load somewhat better than the flat face flange.

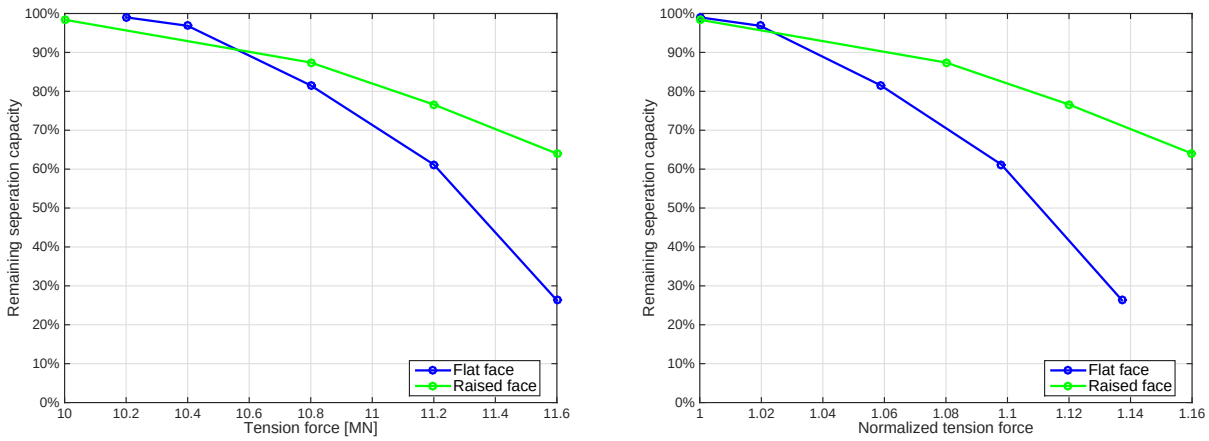

Figure 4.10: *The PLOP in Tension.*

Table 4.5: The resulting PLOP for bending of raised face flange.

Load [kNm]	Remaining capacity
1180	99.1%
1260	94.4%
1340	87.1%
1420	79.4%
1500	70.4%
1580	58.2%
1660	38.4%

Table 4.6: The resulting PLOP for bending of flat face flange.

Load [kNm]	Remaining capacity
1360	98.5%
1400	97.7%
1480	95.8%
1600	89.1%
1740	72.9%
1900	45.5%
2200	0

Figure 4.11 illustrates the remaining preload capacity after various magnitudes of bending moment. After normalization of the curves, it can be seen that the flanges exhibit a similar behaviour, although the flat face flange can withstand a higher bending moment.

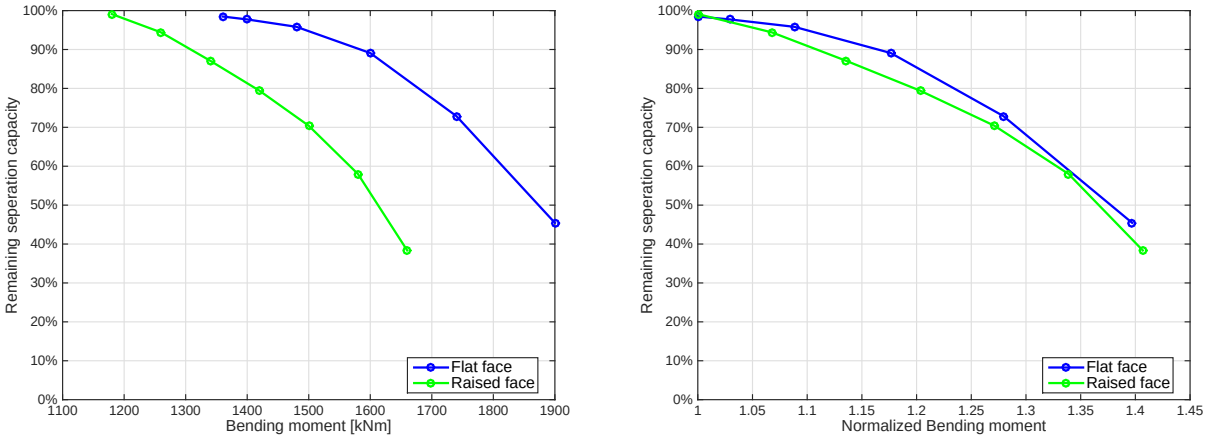

Figure 4.11: *The PLOP in bending.*

In table 4.7 and table 4.8, the remaining separation capacities for the raised face flange and the flat face flange are presented respectively when subjected to various magnitudes of internal pressure. The corresponding behaviour is plotted in fig. 4.12.

Table 4.7: The resulting PLOP for pressure of raised face flange.

Load [MPa]	Remaining capacity
195	98.4%
200	97.3%
205	94.1%
210	92.0%
215	87.2%

Table 4.8: The resulting PLOP for pressure of flat face flange.

Load [MPa]	Remaining capacity
212	98.4%
214	96.9%
216	95.5%
218	91.8%

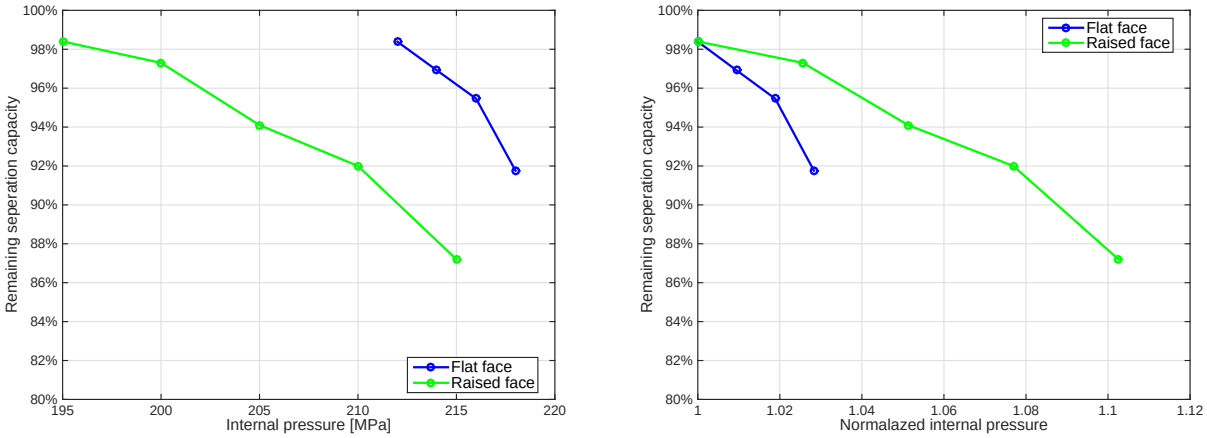

Figure 4.12: *The PLOP in pressure.*

4.3 Capacities of combined loads

The capacities when the flange are subjected to a combination of tension, bending and internal pressure can be linearly interpolated using eq. (3.4). For simplicity, the design factor F_d is set to 1. This gives:

$$\frac{T}{T_c} + \frac{M}{M_c} + \frac{p}{p_c} \leq 1$$

This linear equation is based on the assumption that the failure mechanics associated with each capacity are fully dependent. This means that if one utilization is increased by $x\%$, the allowable total utilization for the other capacities has to be decreased by $x\%$ to remain safe. The units of force, moment and pressure are kN, kNm and MPa respectively.

4.3.1 Combined structural capacities

The structural capacity for the raised face flange is defined as:

$$\frac{T}{11848} + \frac{M}{2070} + \frac{p}{230} \leq 1 \tag{4.1}$$

and the corresponding capacity for the flat face flange is:

$$\frac{T}{11846} + \frac{M}{2916} + \frac{p}{233} \leq 1 \tag{4.2}$$

By considering the utilization of each capacity as one variable, the capacity equations can be drawn in 3D space, see fig. 4.13. The safe region is limited by the tetrahedral volume.

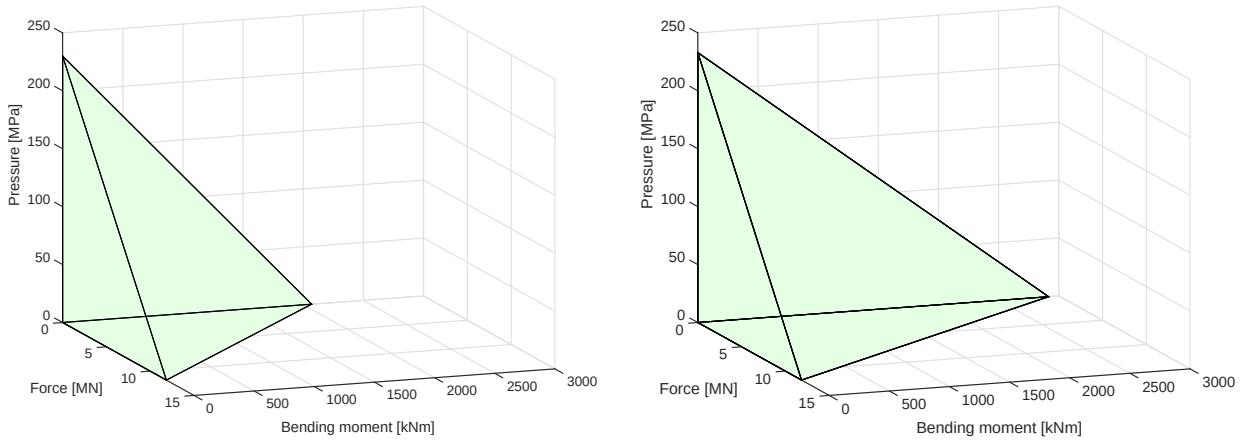

(a) *Raised face.* (b) *Flat face.*

Figure 4.13: *Combined structural capacities.*

4.3.2 Combined leakage capacities

Due to requests from Aker Solutions the leakage capacities were removed from the combined leakage capacities. The values are replaced with $T_{leak}, M_{leak}, p_{leak}$ representing the leakage load in tension, bending and internal pressure respectively. The leakage capacity for the raised face flange is defined as:

$$\frac{T}{T_{leak}} + \frac{M}{M_{leak}} + \frac{p}{p_{leak}} \leq 1 \tag{4.3}$$

and the corresponding capacity for the flat face flange is:

$$\frac{T}{T_{leak}} + \frac{M}{M_{leak}} + \frac{p}{p_{leak}} \leq 1 \tag{4.4}$$

The combined leakage capacities for the flat face and raised face flange are drawn in 3D space in fig. 4.14 by considering each capacity as one variable. In order to prevent leakage, the load vector $\mathbf{F} = [\text{Tension, Bending, Pressure}]$ must be inside or at the tetrahedral's surfaces.

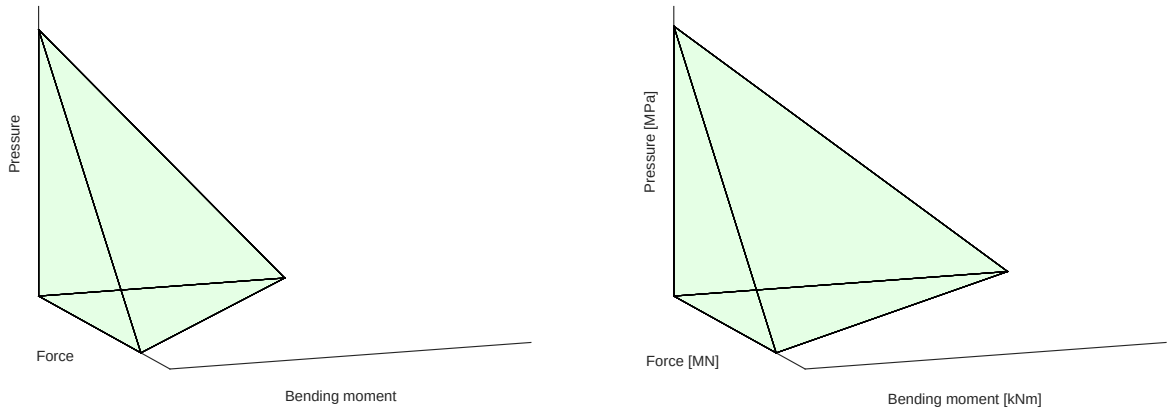

(a) *Raised face.* (b) *Flat face.*

Figure 4.14: *Combined leakage capacities.*

4.3.3 Combined hub face separation capacities

The hub face separation capacity for the raised face flange is defined as:

$$\frac{T}{9800} + \frac{M}{1028} + \frac{p}{188} \leq 1 \tag{4.5}$$

and the corresponding capacity for the flat face flange is:

$$\frac{T}{10120} + \frac{M}{1320} + \frac{p}{211} \leq 1 \tag{4.6}$$

The combined separation capacities for the flat face and raised face flange are drawn in 3D space in fig. 4.15 by considering each capacity as one variable. In order to prevent separation, the load vector $\mathbf{F} = [\text{Tension, Bending, Pressure}]$ must be inside or at the tetrahedral's surfaces.

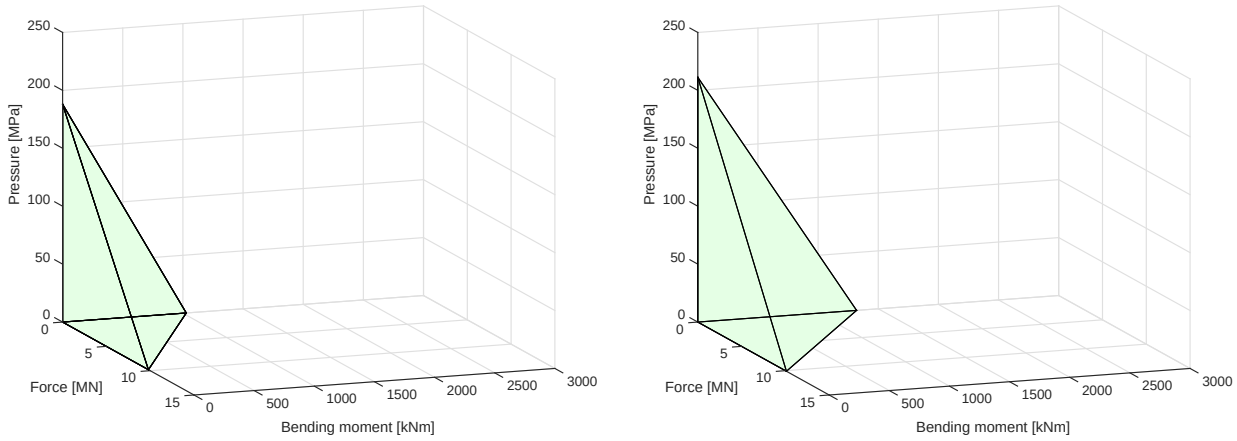

(a) *Raised face.* (b) *Flat face.*

Figure 4.15: *Combined hub face separation capacities.*

4.4 Fatigue

The results from the fatigue analysis are presented in this section. The maximum bending moment range was 680 kNm. Although, this being a relatively high moment range, it gave a high number of cycle to failure. In order to be able to estimate the fatigue life of the flanges, the hot spots must be identified. The hot spots are the critical areas where the cracks will most likely grow. The hot spot in each component was analysed with respect to the maximum effective stress in the integration point from where the stresses were used to estimate the fatigue life. It should be mentioned that based on the maximum stress in the normal direction of the anticipated crack growth direction, i.e. the direction of the maximum principal stress, and the maximum axial stress, the hot spots were located in the same area. Figure 4.16 shows the location of the hot spots in the upper and lower flange from where the stresses were used to estimate the fatigue life. The *M-N* curves were created using the code attached in appendix C.1. The multiaxial stress states were converted to equivalent uniaxial stress states using the code attached in appendix C.2

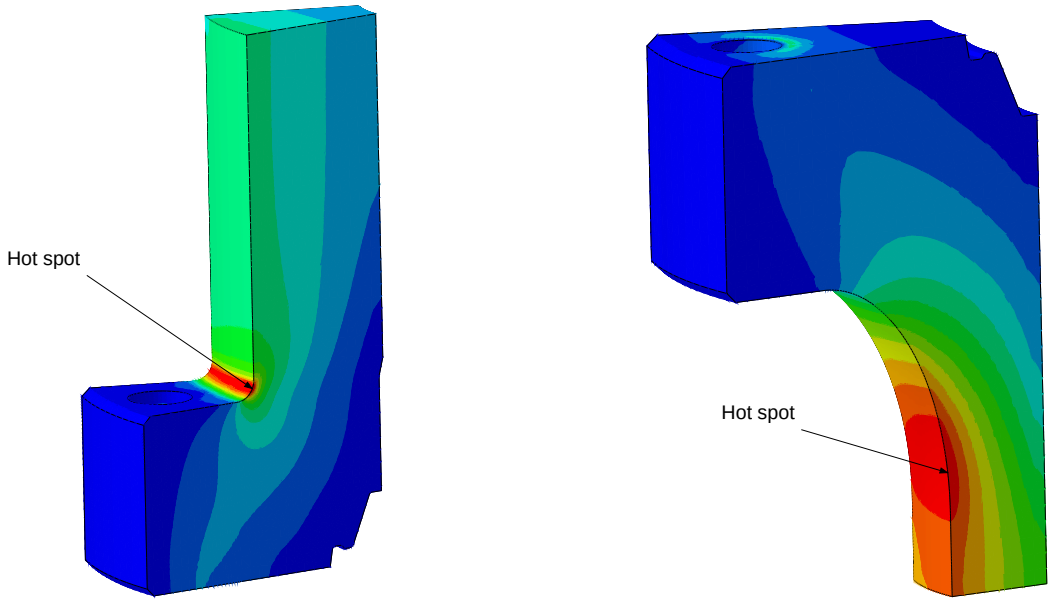

(a) *Upper flange.* (b) *Lower flange.*

Figure 4.16: *The hot spots in the upper and lower flange.*

The fatigue life for different stress ranges in the flanges was calculated according to eq. (3.10). As stated in section 2.6.2 the directions of the principal stresses must remain constant during loading which they did in the present case.

The results for the flat face and the raised face flange are plotted as *M-N* curves in fig. 4.17 and fig. 4.18 respectively. The equivalent stress obtained from eq. (3.9) was equal to the von Mises stress calculated in Abaqus and thus the same *M-N* curve was obtained for both methods.

For the upper flange, the maximum principal stress pointed in the same direction as the normal direction of the anticipated crack growth direction, i.e the tangential direction in the radius and it was higher than the von Mises and the axial stress. This implied that the maximum principal stress had a bigger impact on crack growth than the two other stresses. Hence, fatigue based on the maximum principal stress occurred sooner for an arbitrary moment range, see fig. 4.17a and fig. 4.18a. For the lower flange, since the radius is larger, the effect of the notch on fatigue is smaller than for the upper flange. As can be seen in fig. 4.17b and fig. 4.18b, the axial stress and maximum principal stress resulted in the same *M-N* curve.

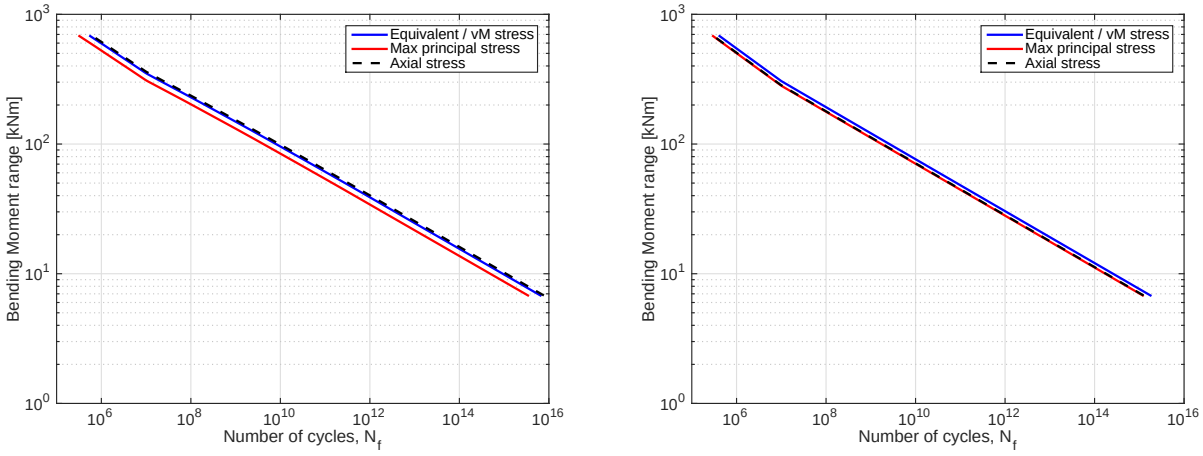

(a) *Upper flange.* (b) *Lower flange.*

Figure 4.17: *M-N curve for flat face flange.*

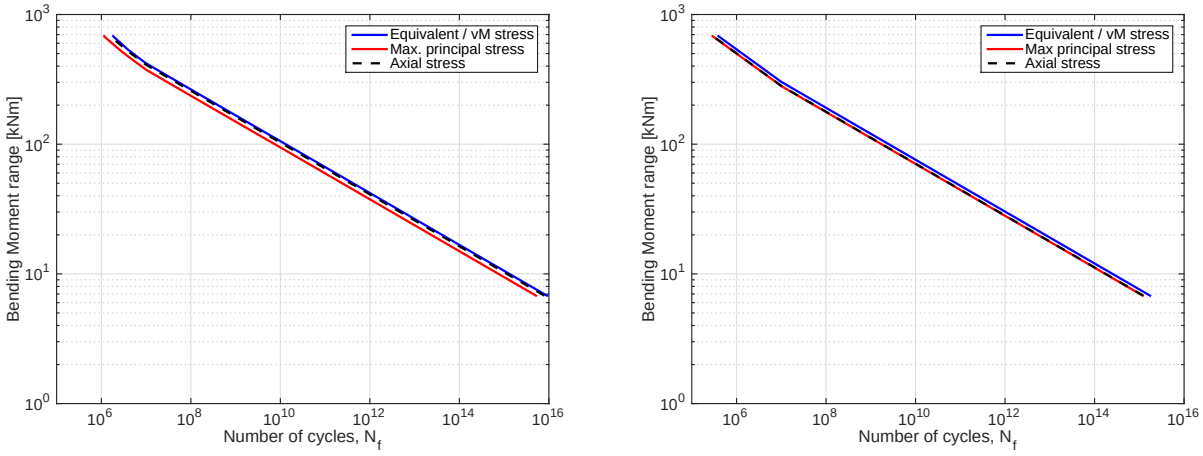

(a) *Upper flange.* (b) *Lower flange.*

Figure 4.18: *M-N curve for raised face flange.*

The *M-N* curves also show that both flanges can handle the same number of load cycles if they are subjected to a cyclic bending moment with a certain amplitude. For both of the flanges, the lower flange was the critical component having a shorter fatigue life compared to the other components, i.e. the upper flange and the bolts. The maximum bending moment range of 680 kNm resulted in a high number of cycle to failure, slightly below 10^6 cycles. This being a relatively high environmental cyclic load would mean that the realistic fatigue life is better.

For the bolts, the results were more difficult to interpret. The highest stress range in the bolt occurred in the threaded region. The use of "tie-coupling" between the bolts and the flange removed the effect of the stress concentration in the threads and at the same time caused a singularity near the edge which increased the stresses in that area. The stresses in the edge reached the yield limit. Another effect was that the stresses obtained in the threaded region were very noisy. The noisy stresses can be seen in fig. 4.19a and the corresponding *M-N* curves are plotted in appendix B. For this reason, the stress ranges used to predict the fatigue life were taken from an area above the edge, see fig. 4.19b.

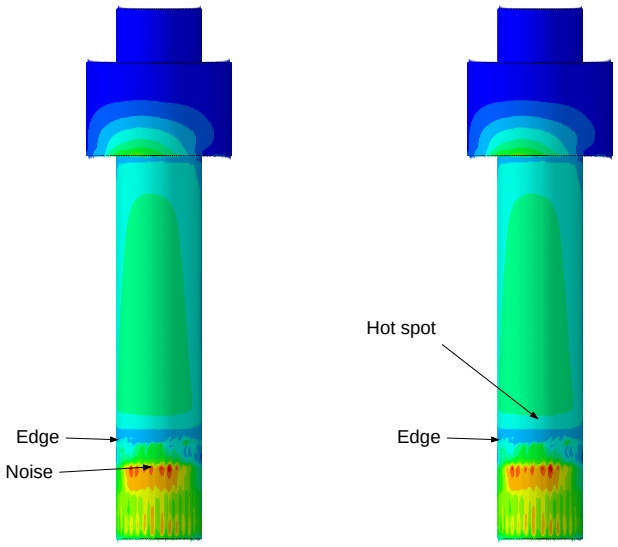

(a) *Noisy stress.* (b) *Hot spot.*

Figure 4.19: *Stress distribution in bolt.*

Using "threaded interaction" between the bolt and the flange gave longer fatigue life. In fig. 4.20, the fatigue lives for the bolt in the raised face flange obtained with different method are plotted as *M-N* curves. As can be seen, the same result was obtained for the different methods.

It may be difficult to see much difference in the plots due to the logarithmic axes, but when evaluating the fatigue life due to a cyclic load of 100 kNm, the fatigue life for the bolt with the "threaded interaction" is $1.69 \cdot 10^{10}$ cycles. This is roughly twice the fatigue life of the bolt with the "tie-constraint" that has a fatigue life of $9.13 \cdot 10^{9}$ cycles.

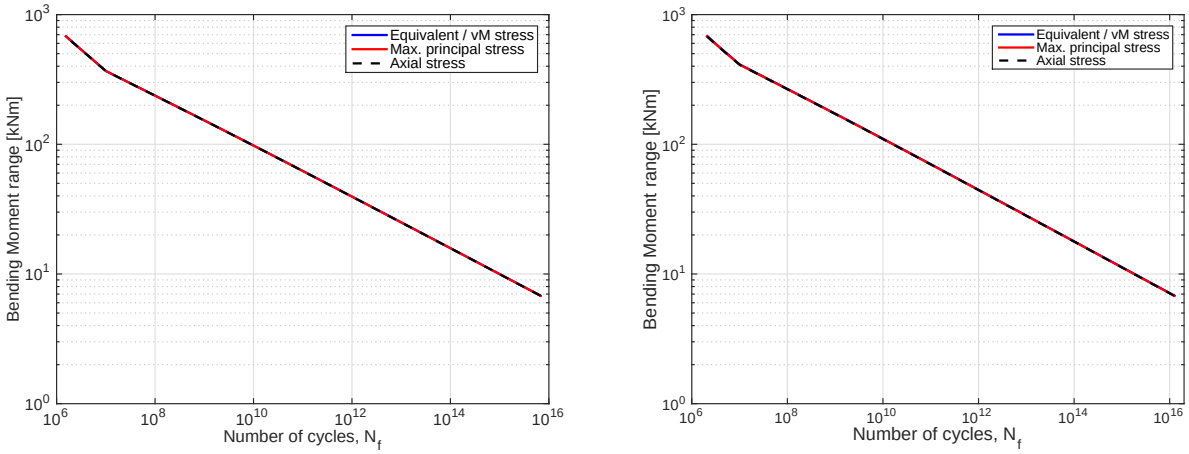

(a) *Tie Constraint.* (b) *Threaded Interaction.*

Figure 4.20: *M-N curve for bolt in raised face flange.*

In fig. 4.21, the *M-N* curves for the bolt in the flat face flange are plotted. For high cyclic bending moment, the curves behave nonlinear which could be due to local yielding in the bolt leading to a nonlinear bending moment-stress relation.

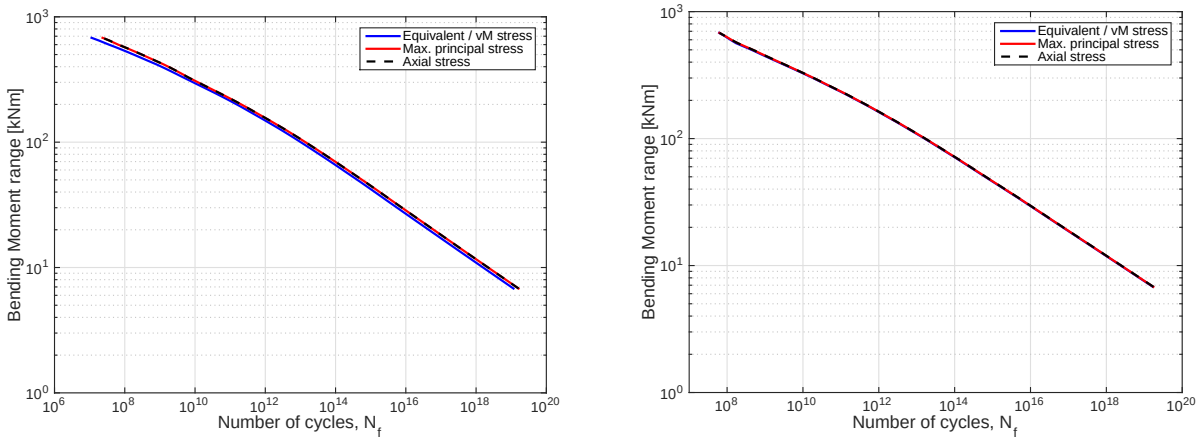

(a) *Tie Constraint.* (b) *Threaded Interaction.*

Figure 4.21: *M-N curve for bolt in flat face flange.*

As stated in an internal best practice document [22], "in some cases, the mean stress level prior to or during fatigue loading is so high that plastic redistribution occurs. One example is a threaded connection where the first thread will initially see the highest load. As the load increases above the yield point, more and more of the load is transferred to the next threads. This will cause a reduction of the calculated peak stress range and thereby give an increase in fatigue life. The methodology recommended in TR 3541 [8] is to apply constant cyclic loads to the model until the stress range is stabilized and then use the stabilized stress range in the fatigue evaluation. According to TR 3541 [8], typically eight to twelve bending moment ranges are recommended. However, it is not necessary to repeat loading when the stress range has stabilized."

This recommendation was implemented where the flange was loaded and unloaded four times to stabilize the stress range. As seen in 4.22a, the stress stabilized in the second loading cycle motivating no further need of additional loading cycles. After stabilization the relation was still nonlinear, even though the strain-stress relation was linear as seen in fig. 4.22b. The nonlinear behaviour is therefore not an effect of the material model, but could be due to initial hub face separation or loss of pre load. Further investigations are needed.

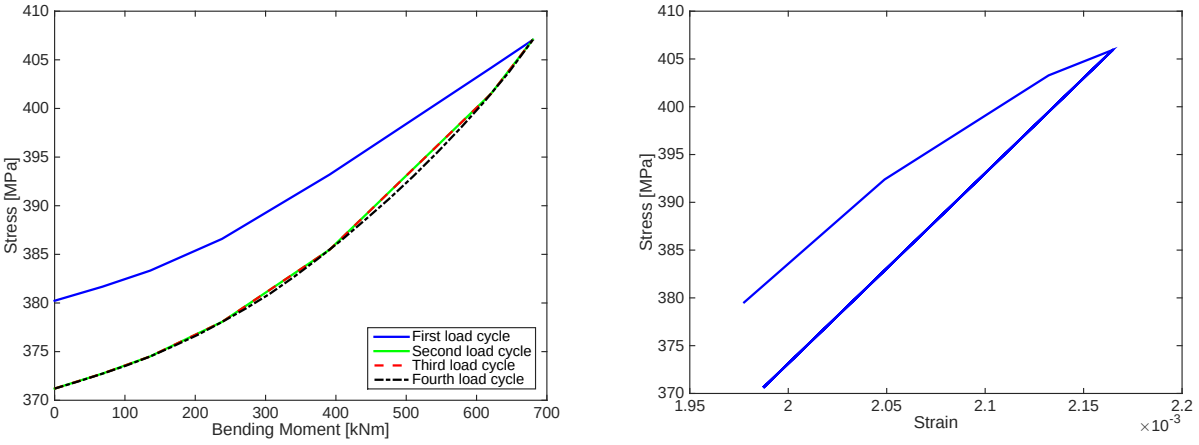

(a) *Moment-stress relationship.* (b) *strain-stress relationship.*

Figure 4.22: *Behaviour of the stress in the bolt during four cycles.*

5 Conclusion

The capacities of two geometrically different flanges used in the oil and gas industry were evaluated according to industrial standards. The capacities were evaluated with respect to structural and functional criteria and the applied loads consisted of tension, bending and internal pressure. Additionally, a high cycle fatigue assessment relating an applied bending moment to the number of cycles to failure was performed. The aim of the project was to identify differences in performance between the two flanges in order to gain a better understanding of the different parameters when designing flanges.

For the structural capacity, the flat face flange could be subjected to a 40% higher bending moment compared with the raised face flange. For the case of tension and internal pressure no significant differences could be seen. The same results could be seen for the functional capacities, the flanges performed similarly when loaded in tension and internal pressure, but when loaded in bending the flat face flange could withstand a greater moment.

When subjected to an alternating bending load, three different hot spots were evaluated; the upper radius, the lower radius and the bolts. For an arbitrary load, the two flanges exhibited similar fatigue properties. In contrast, the bolts on the flat face flange performed superior to the corresponding part on the raised face flange. Although, as a complete assembly, the flange would fail first due to shorter fatigue life.

The results from this project suggest that the capacities of the flat face flange are greater than the capacities of the raised face flange when the present criteria and methods are used. This is motivated due to the fact that all capacities are equal or better for the flat face flange.

Other aspects of consideration includes the difference in manufacturing tolerances for the flanges. The hub faces of the flat face flange are more sensitive to surface skewness and therefore demand a higher precision in flatness for the contacting hub faces. The larger contact area of the flat face flange is also more sensitive to surface scratches, paint and other imperfections that could occur during manufacturing or assembly.

5.1 Future work

To further improve the presented analyses a number of additional considerations and improvements should be made. As stated in section 3.2.5 the bolts were pretensioned to 67% of the yield strength. To capture the scatter or uncertainty of the preload and identify the sensitivity of the flange connection to an incorrect preload, the analyses should be remade with different preloads.

As seen in section 4.4, considerable noise existed in the bolts, especially in the threads, when evaluating the fatigue properties. For an improved fatigue analysis this noise should be minimized. To do this, it is recommended to have a matching element size on the bolts and on the flange holes. If possible, the threads should be submodelled in detail in order to better capture the stress field. Considering the bending moment-stress relation in the bolt for the flat face flange, further investigations have to be done to find the reason for the nonlinear behaviour at high values of bending moment range.

The nuts and studs were modelled as one complete part, as described in section 3.1.2, not considering the threads in the interface between the nut and stud. For an improved analysis, this interface should also be considered.

When calculating the capacity in combined loading, a linear interpolation was used. Although this is a conservative method, a future analyse should calculate the capacities for combined loads specifically. In addition, the behaviour of axial compression as well as external overpressure should be investigated.

Due to the inconsistency between the pressure and force criterion seen in section 4.2.2 and the large plastic strains in the seal seen in section 4.1.3, further examination of the behaviour of the seal during internal pressure should be considered.

References

[1] Sawa, Toshiyuki, Hiroyuki Kumano, and Hirofumi Iwakawa. (1986). On the characteristics of bolted joins with gaskets, (Stress analysis of metallic gaskets with raised face interposed between pipe flanges). *Bulletin of JSME* **25**, 385–392.

[2] Alghamdi, Abdulmalik A. and Muhsen S. Al-Sannaa. (2004). Two-Dimensional Finite Element Analysis for Large Diameter Steel Flanges. *Journal of Pressure Vessel Technology* **126**, 399–403.

[3] Mathan, G. and N. Siva Prasad. (2011). Studies on gasketed flange joints under bending with anisotropic Hill plasticity model for gasket. *International Journal of Pressure Vessels and Piping* **88**, 495–500.

[4] Takagi, Yoshio et al. (2013). FEM Stress Analysis and the Sealing Performance Prediction of Pipe Flange Connections under External Bending Moments and Internal Pressure. *Journal of Solid Mechanics and Material Engineering* **7** (4), 486–495.

[5] Sawa, Toshiyuki, Wataru Maezaki, and Satoshi Nagata. (2004). "Stress Analysis and the Sealing Performance Evaluation of Pipe Flange Connections With Gaskets Subjected to Internal Pressure and External Bending Moment: Effects of Scatter in Bolt Preload". *ASME/JSME 2004 Pressure Vessels and Piping Conference*. Prague, Czech Republic, pp. 137–143. ISBN: 0-7918-4673-3.

[6] Sawa, T., N. Higurashi, and H. Akagawa. (1991). A Stress Analysis of Pipe Flange Connections. *J. Pressure Vessel Technol* (4), 497–503.

[7] *Petroleum and natural gas industries - Design and operation of subsea production systems - Part 7: Completion/workover riser systems (ISO 13628-7:2005)*. (2005). International Organization for Standardization.

[8] *Drilling and well, Technical and proffessional requirement,TR 3541*. (2005). Statoil.

[9] *Fatigue Design of Offshore Steel Structures, Recomended Practice DNV-RP-C203*. (2010). Det Norske Veritas.

[10] Lillebø, Bjarte. (2006). "Bolting materials subsea". *Materials in Offshore Construction Conference*. Det Norske Veritas. Esbjerg.

[11] Smolnicki, T., E. Rusinski, and J. Karlinski. (2007). FEM modelling of fatigue loaded bolted flange joints. *Journal of Achievements in Materials and Manufacturing Engineering* **22** (1), 69–72.

[12] Jesus, Abílio M.P. de et al. (2012). A comparison of the fatigue behavior between S355 and S690 steel grades. *Journal of Constructional Steel Research* **79** (4), 140–150. DOI: 10.1016/j.jcsr.2012.07.021.

[13] Mägi, Mart and Kjell Melkersson. (2011). *Lärobok i Maskinelement*. Johanneshov: MTM.

[14] Ottosen, Niels and Hans Petersson. (1992). *Introduction to the Finite Element Method*. New York: Prentice Hall. ISBN: 0-13-473877-2.

[15] Hazewinkel, Michiel. (2001). *Galerkin method*. Houten, NL: Springer. ISBN: 978-1-55608-010-4.

[16] *Abaqus 6.13 Online Documentation*. (2013). Dassault Systèmes.

[17] Sun, Eric Qiulu. Shear Locking and Hourglassing in MSC Nastran, ABAQUS, and ANSYS.

[18] Runesson, Kenneth. *Constitutive modeling of engineering materials - Theory and computations*. Dept. of Applied Mechanics, Chalmers University of Technology.

[19] Dowling, Norman E. (2013). *Mechanical Behavior of Materials*. 4th ed. Upper Saddle River, NJ: Pearson Education Limited. ISBN: 978-0-273-76455-7.

[20] Papuga, Jan, Miguel Vargas, and Martin Hronek. (2012). Evaluation of Uniaxial Fatigue Criteria Applied to Multiaxially Loaded Unnotched Samples. *Engineering Mechanics* **19** (2/3), 99–111.

[21] Montgomery, Jerome. (2008). "Boundary Condition Influences on Shank Stress in 3D Solid Bolt Simulation". *Abaqus Users Conference*. Siemens Generation Inc. Orlando,FL.

[22] *Analysis Best Practice WOS ISO 13628-7 Riser Connectors*. (2005). Aker Solutions.

Appendix A Mesh convergence study for flange radius

Figure A.1 displays how the von Mises stress converges when the element size in the upper radius is decreased.

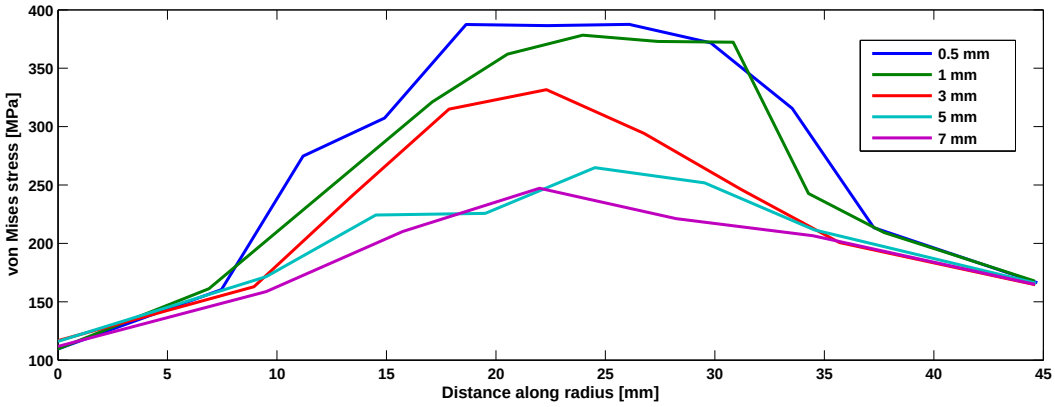

Figure A.1: *The stress in the upper radius for different element sizes.*

Appendix B M-N curves for different hot spots on bolt

The *M-N* seen in figures B.2 and B.3 were obtained by evaluating the stress range in the threaded area in the bolt, see fig. B.1.

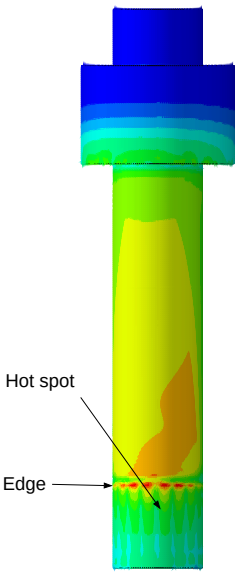

Figure B.1: *The stress in the upper radius for different element sizes.*

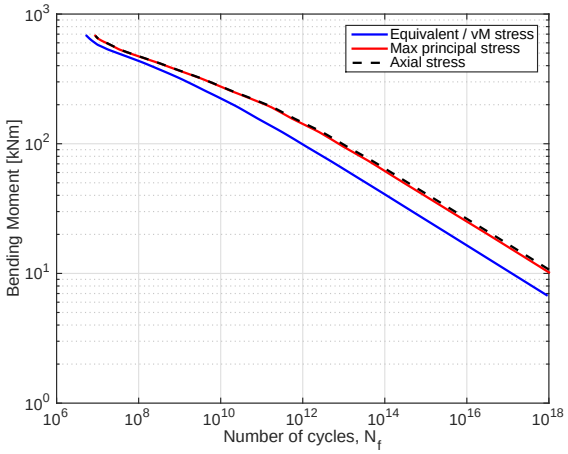

(a) *Tie Constraint.*

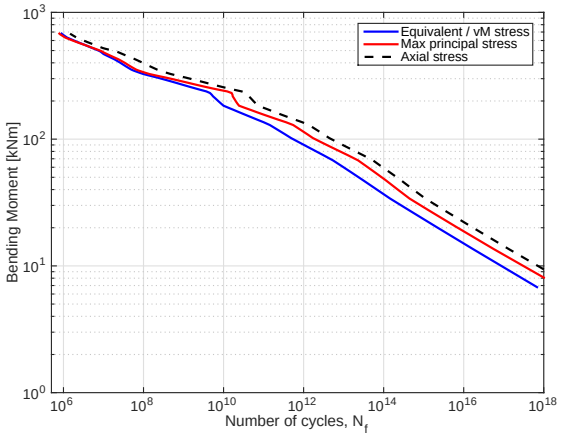

(b) *Threaded Interaction.*

Figure B.2: *M-N curve for bolt in flat face flange.*

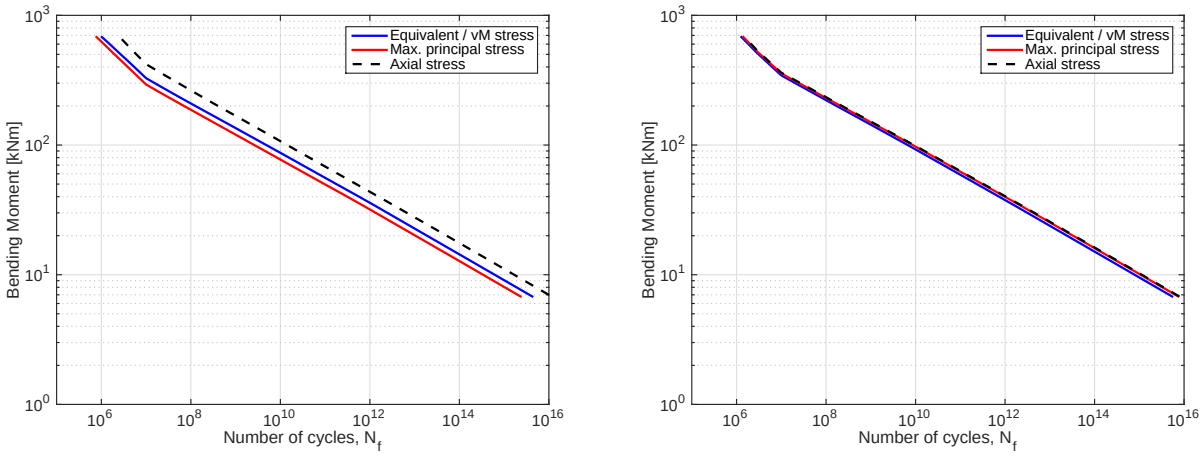

(a) *Tie Constraint*

(b) *Threaded Interaction*

Figure B.3: *M-N curve for bolt in raised face flange.*

Appendix C Matlab code

C.1 Fatigue life estimator

```
function [S,N]=SN(curve,S,t,t_ref,k)
% SN calculates and plots the fatigue life (S-N) curve for seamless pipes
% and Cold-rolled bolts.
% Call:
%   SN('curve',S)
%   SN('curve',S,t,t_ref,k)
% ------------------------------------------------------
%   S:            Stress range vector
%   Curve:        S-N curve from test
%                   - B1 for seamless pipe
%                   - F1 for bolt (Cold-rolled)
%   t:            Thickness through which a crack will
%                 most likely grow:
%                   - 43.5 mm for bolt
%                   - 126.045 mm for seamless pipe
%   t_ref:        Reference thickness
%                   - 25 mm for bolt
%                   - 32 mm for seamless pipe
%   k:            Thickness exponent
%                   - 0.25 for F1
%                   - 0 for B1
% ------------------------------------------------------
if nargin==2
    switch curve
        case 'B1'
            for i=1:length(S)
                if S(i)<=106.97
                    m=5; % negative inverse slope of S-N curve
                    loga=17.146;  % intercept of log N-axis by S-N curve
                else
                    m=4;
                    loga=15.117;
                end
                logN(i)=loga-m*log10(S(i));
                N(i)=10^logN(i); % Predicted number of cycles to failure
            end
        case 'F1'
            for i=1:length(S)
                if S(i)<=36.84
                    m=5;
                    loga=14.832;
                else
                    m=3;
                    loga=11.699;
                end
                logN(i)=loga-m*log10(S(i));
                N(i)=10^logN(i);
            end
        otherwise disp('Wrong curve name, must use F1 or B1!!')
    end
else % effect of plate thickness and strcural stress concentration factor
    switch curve
        case 'B1'
            for i=1:length(S)
                if S(i)<=106.97
                    m=5;
                    loga=17.146;
                else
                    m=4;
                    loga=15.117;
                end
                logN(i)=loga-m*log10(S(i)*(t/t_ref)^k);
```

```
                N(i)=10^logN(i);
            end
        case 'F1'
            for i=1:length(S)
                if S(i)<=36.84
                    m=5;
                    loga=14.832;
                else
                    m=3;
                    loga=11.699;
                end
                logN(i)=loga-m*log10(S(i)*(t/t_ref)^k);
                N(i)=10^logN(i);
            end
    end
end
end
```

C.2 Equivalent stress calculator

```
function [dsig_eq]=sig_eq(method,sig_1,sig_2,sig_3,sig_vM)
% sig_eq converts a multiaxial state of stress to an equivalent unaxial
% stress
% Call:
% [dsig_eq]=sig_eq(method,sig_1,sig_2,sig_3)
% [dsig_eq]=sig_eq(method,sig_vM)
% ------------------------------------------------------
% method:           vonMises or Manson-Mcknight
% sig_1:            Maximum principle stress
% sig_2:            Mid principle stress
% sig_3:            Minimum principle stress
% sig_vM:           von Mises stress
% ------------------------------------------------------
if nargin==4 | nargin==5 | nargin==2
    switch method
        case 'Manson-McKnight'
            for i=1:length(sig_1)
                dsig_eq(i,1)=sqrt((sig_1(i)-sig_2(i))^2+(sig_1(i)-sig_3(i))^2+...
                    (sig_2(i)-sig_3(i))^2)/sqrt(2);
            end
        case 'vonMises'
            dsig_eq=sig_vM;
    end
end
end
```